

## Interplanetary Magnetic Flux Rope Observed at Ground Level by HAWC

```
S. Akiyama<sup>1</sup>, R. Alfaro<sup>2</sup>, C. Alvarez<sup>3</sup>, J. R. Angeles Camacho<sup>2</sup>, J. C. Arteaga-Velázquez<sup>4</sup>, K. P. Arunbabu<sup>5</sup>, D. Avila Rojas<sup>2</sup>,
       H. A. Ayala Solares<sup>6</sup>, E. Belmont-Moreno<sup>2</sup>, K. S. Caballero-Mora<sup>3</sup>, T. Capistrán<sup>7</sup>, A. Carramiñana<sup>7</sup>, S. Casanova<sup>8</sup>,
 P. Colin-Farias<sup>5,9</sup>, U. Cotti<sup>4</sup>, J. Cotzomi<sup>10</sup>, E. De la Fuente<sup>11</sup>, C. de León<sup>4</sup>, R. Diaz Hernandez<sup>7</sup>, C. Espinoza<sup>2</sup>, N. Fraija<sup>12</sup>,
A. Galván-Gámez<sup>12</sup>, D. García<sup>2</sup>, J. A. García-González<sup>2</sup>, F. Garfias<sup>12</sup>, M. M. González<sup>12</sup>, J. A. Goodman<sup>13</sup>, J. P. Harding<sup>14</sup>, B. Hona<sup>15</sup>, D. Huang<sup>15</sup>, F. Hueyotl-Zahuantitla<sup>3</sup>, P. Hüntemeyer<sup>15</sup>, A. Iriarte<sup>12</sup>, V. Joshi<sup>16</sup>, D. Kieda<sup>17</sup>, G. J. Kunde<sup>14</sup>, A. Lara<sup>5</sup>, H. León Vargas<sup>2</sup>, G. Luis-Raya<sup>18</sup>, K. Malone<sup>14</sup>, J. Martínez-Castro<sup>19</sup>, J. A. Matthews<sup>20</sup>, P. Miranda-Romagnoli<sup>21</sup>, E. Moreno<sup>10</sup>,
A. Nayerhoda<sup>8</sup>, L. Nellen<sup>22</sup>, M. Newbold<sup>17</sup>, T. Niembro<sup>23</sup>, T. Nieves-Chinchilla<sup>24</sup>, R. Noriega-Papaqui<sup>21</sup>, E. G. Pérez-Pérez<sup>18</sup>,
         L. Preisser<sup>5</sup>, C. D. Rho<sup>25</sup>, J. Ryan<sup>26</sup>, H. Salazar<sup>10</sup>, F. Salesa Greus<sup>8</sup>, A. Sandoval<sup>2</sup>, R. W. Springer<sup>17</sup>, I. Torres<sup>7</sup>,
                                                              F. Ureña-Mena<sup>7</sup>, L. Villaseñor<sup>10</sup>, and A. Zepeda<sup>27</sup>
The Catholic University of America, Washington, DC, USA
                                           <sup>2</sup> Instituto de Física, Universidad Nacional Autónoma de México, Ciudad de México, Mexico
                                                           Universidad Autónoma de Chiapas, Tuxtla Gutiérrez, Chiapas, Mexico
                                                         4 Universidad Michoacana de San Nicolás de Hidalgo, Morelia, Mexico
      <sup>5</sup> Instituto de Geofísica, Universidad Nacional Autónoma de México, Ciudad de México, Mexico; arun@igeofisica.unam.mx, alara@igeofisica.unam.mx
                                                    Department of Physics, Pennsylvania State University, University Park, PA, USA
                                                           Instituto Nacional de Astrofísica, Óptica y Electrónica, Puebla, Mexico
                                         <sup>8</sup> Institute of Nuclear Physics, Polish Academy of Sciences, PL-31342 IFJ-PAN, Krakow, Poland
                                 9 Posgrado en Ciencias de la Tierra, Universidad Nacional Autónoma de México, Ciudad de México, Mexico
                                     Facultad de Ciencias Físico Matemáticas, Benemérita Universidad Autónoma de Puebla, Puebla, Mexico
                  <sup>11</sup> Departamento de Física, Centro Universitario de Ciencias Exactas e Ingenierías, Universidad de Guadalajara, Guadalajara, Mexico
                                          Instituto de Astronomía, Universidad Nacional Autónoma de México, Ciudad de México, Mexico
                                                         Department of Physics, University of Maryland, College Park, MD, USA
                                                     <sup>14</sup> Physics Division, Los Alamos National Laboratory, Los Alamos, NM, USA
                                                  <sup>15</sup> Department of Physics, Michigan Technological University, Houghton, MI, USA
                            <sup>16</sup> Erlangen Centre for Astroparticle Physics, Friedrich-Alexander-Universität Erlangen-Nürnberg, Erlangen, Germany
                                                  Department of Physics and Astronomy, University of Utah, Salt Lake City, UT, USA
                                                              <sup>18</sup> Universidad Politécnica de Pachuca, Pachuca, Hidalgo, Mexico
                                     19 Centro de Investigación en Computación, Instituto Politécnico Nacional, Ciudad de México, Mexico
                                                 Dept of Physics and Astronomy, University of New Mexico, Albuquerque, NM, USA

21 Universidad Autónoma del Estado de Hidalgo, Pachuca, Mexico
                                  Instituto de Ciencias Nucleares, Universidad Nacional Autónoma de México, Ciudad de México, Mexico
Smithsonian Astrophysical Observatory, Cambridge, MA, USA
                                                        <sup>24</sup> Heliosphysics Science Division, NASA-GSFC, Washington, DC, USA
                                                                           University of Seoul, Seoul, Republic of Korea <sup>26</sup> University of New Hampshire, NH, USA
              <sup>27</sup> Departamento de Física, Centro de Investigación y de Estudios Avanzados del Instituto Politécnico Nacional, Ciudad de México, Mexico
                              Received 2020 September 18; revised 2020 October 14; accepted 2020 October 19; published 2020 December 15
```

### **Abstract**

We report the ground-level detection of a Galactic cosmic-ray (GCR) flux enhancement lasting  $\sim$ 17 hr and associated with the passage of a magnetic flux rope (MFR) over the Earth. The MFR was associated with a slow coronal mass ejection (CME) caused by the eruption of a filament on 2016 October 9. Due to the quiet conditions during the eruption and the lack of interactions during the interplanetary CME transport to the Earth, the associated MFR preserved its configuration and reached the Earth with a strong magnetic field, low density, and a very low turbulence level compared to local background, thus generating the ideal conditions to redirect and guide GCRs (in the  $\sim$ 8–60 GV rigidity range) along the magnetic field of the MFR. An important negative  $B_Z$  component inside the MFR caused large disturbances in the geomagnetic field and a relatively strong geomagnetic storm. However, these disturbances are not the main factors behind the GCR enhancement. Instead, we found that the major factor was the alignment between the MFR axis and the asymptotic direction of the observer.

*Unified Astronomy Thesaurus concepts*: Cosmic rays (329); Solar coronal mass ejections (310); Interplanetary medium (825); Interplanetary magnetic fields (824); Interplanetary particle acceleration (826)

## 1. Introduction

The modulation of the Galactic cosmic-ray (GCR) flux by solar activity has been known and studied since the 1930s, after the discovery of these extraterrestrial particles (see Lockwood 1971, for a historical review of this subject). The Parker theory of transport (Parker 1965) has been successfully applied to explain the "long-term modulation," i.e., the observed anticorrelation between the sunspot number and the GCR flux on the timescale of the solar magnetic cycle (22 yr, Ferreira & Potgieter 2004).

Moreover, analyzing direct measurements of the interplanetary magnetic field over an entire solar cycle, Duggal et al. (1983) reached the conclusion that GCR intensity increases and decreases where associated with weak and strong interplanetary magnetic fields, respectively.

On shorter timescales (weeks or days) the modulation is driven by disturbances such as coronal mass ejections (CMEs), which are large amounts of magnetized plasma ( $\sim 10^{15}$  g, Colaninno & Vourlidas 2009) expelled from the low corona to

the interplanetary medium with speeds ranging from  $\sim 100$  to  $\sim 3000 \, \mathrm{km \, s^{-1}}$ . At low coronal levels, the major events associated with CMEs are flares (Schmieder et al. 2015) and filament eruptions (Sinha et al. 2019); the latter, also known as prominences, constitute the tracers of helical flux ropes in the corona (Filippov et al. 2015).

The interplanetary counterparts of CMEs (ICMEs) can be recognized by their structure: a leading shock wave, followed by a turbulent sheath region and the driving ejecta (Luhmann et al. 2020). A particular subset of ICMEs (up to 77% according to Nieves-Chinchilla et al. 2019) shows a clear rotation of the magnetic field components corresponding to a magnetic flux rope (MFR) structure known as a magnetic cloud (MC, Burlaga et al. 1981). From the space—weather point of view, ICMEs have deserved great attention due to their potential effects on the Earth's magnetic field and the associated risk to space-based technology. These effects are known as "geo-effectiveness" and are generally measured by geomagnetic indices such as the so-called disturbance storm-time ( $D_{\rm ST}$ ) index. <sup>28</sup>

It is widely accepted that ICMEs may cause decrements of the GCR flux known as Forbush decreases (FDs, Forbush 1937). Extensive literature has been devoted to the detailed study of the effects of ICME internal structure on the GCR intensity (e.g., Snyder et al. 1963; Sarp et al. 2019; Light et al. 2020, and references therein). In particular, there is no consensus about the role that the shock, the sheath, and the MC play in the modulation (Cane 2000; Richardson & Cane 2011). Furthermore, the not-uncommon magnetic field topology of a helical flux tube or helical flux tube and MFR are the same thing. MFR has been poorly studied, particularly in terms of the possibility of how the force-free and helical geometry affects the local GCR population by redirecting and guiding GCRs if the turbulence intensity is low (Belov et al. 2015).

On timescales of hours, GCR enhancements have been detected before the arrival of CMEs; these are the so-called precursors and are attributed to a loss-cone mechanism (Munakata et al. 2000; Rockenbach et al. 2011). Besides, enhancements of the GCR intensity have been observed during geomagnetic storms since the 1950s (Yoshida 1959). Soon thereafter, it was noticed that these increases were not caused by solar energetic particles (related to flares), nor by anomalies of the diurnal anisotropy; neither were they due to changes in the cutoff rigidity caused by the variations of the geomagnetic field (Kondo et al. 1960). Altukhov et al. (1963) outlined the possibility that a "magnetic tongue" rooted in the Sun was causing the observed GCR enhancements (see Duggal & Pomerantz 1962, for more proposed mechanisms). Nevertheless, the poor knowledge of the ICME structure at that time prevented the advance of the investigations, and the subject was somehow forgotten.

An important GCR enhancement was observed in 2016 October by the High Altitude Water Cerenkov array (HAWC), and in this work we present evidence that this excess was due to an anisotropic GCR flux caused by the MFR. The size and the energy range of HAWC (Section 2) enabled the detection of this enhancement, which was less than  $\sim 1\%$  with respect to the

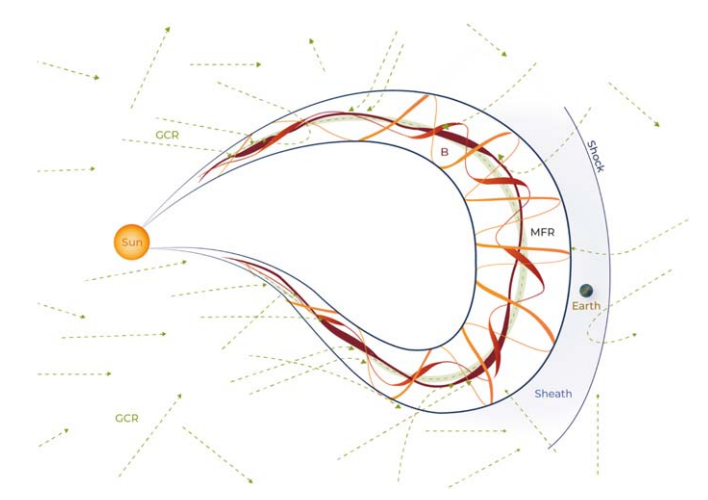


**Figure 1.** Schematic representation of an interplanetary MFR (the field magnitudes are represented by different reddish color bands, the darker and thicker bands corresponding to a stronger magnetic field) arriving at the vicinity of the Earth. The GCRs (dashed green lines) are deflected by the helical magnetic field and guided along the MFR axis.

mean GCR flux for rigidities >8 GV, a marginal signal at best for the neutron monitor (NM) network.

Besides the high sensitivity of HAWC, we propose that three major factors contributed to this unprecedented observation. Therefore we explain each of those factors in detail, namely:

- 1. The solar origin of the MFR was a "quiet" filament eruption (i.e., without an associated flare), resulting in a slow CME ( $\sim$ 180 km s<sup>-1</sup>) launched on 2016 October 9 (Section 3.1 and see Nitta & Mulligan 2017).
- 2. The MFR reached 1 au without being seriously distorted or disrupted, preserving a regular geometry and low turbulence level. Due to the lack of observations between the Sun and 1 au, we performed 2D hydrodynamic simulations of the interplanetary transport of the MFR (Section 3.4) and found that the associated ICME transport was surrounded, front and back, by two highspeed streamers (HSSs, Snyder et al. 1963; Sheeley et al. 1976), but without interacting with them, preserving the helical geometry properties of the MFR at 1 au (Section 3.2).
- 3. The impact of the MFR on the Earth's magnetosphere was observed by a constellation of near-Earth spacecraft. The low flow pressure combined with the large south  $B_Z$  component of the field in the MFR produced intense and moderate disturbances of the magnetosphere the day before and during the HAWC observations respectively (Section 3.5). This lack of correlation shows that the geomagnetic disturbances are not the main causes of the HAWC observation.
- 4. The main factor that allowed detection at ground level is the alignment between the MFR axis and the asymptotic direction of the detector (Section 4.2).

With the absence of significant solar activity, a marginal registration of the event in the NM network, and no other corroborating high-energy signal, one would normally relegate the HAWC signal to a category of unexplained features. However, due to the confluence of several heliospheric conditions, we suggest a model in which the GCRs are guided along the MFR axis (a schematic of this scenario is shown in Figure 1), which can explain the phenomenon. As stated, the

 $<sup>^{\</sup>overline{28}}$  "The  $D_{ST}$  index is related to the average of the longitudinal component of the magnetic external field measured at the equator and surface of the Earth assumed as a dipole" (Sugiura 1964). We recommend the reading of Manchester et al. (2017), Kilpua et al. (2017), Luhmann et al. (2020) and all references therein for further information about the connections between MFRs, CMEs, ICMEs, and MCs.

model relies on these several conditions and we justify each of them via observation or simulation, the key ones being listed above.

To support our findings, we have fitted an MFR model to the in situ observations using the circular-cylindrical model (Nieves-Chinchilla et al. 2016). Then, with the fitted MFR parameters, we computed the trajectory of the GCRs inside the MFR and found a good match (in time and energy) between the trajectories of the GCRs guided inside the MFR and the GCR enhancements observed by HAWC (Section 4). Finally, the discussion and our conclusions are presented in Sections 5 and 6.

### 2. HAWC and Its Observation of a Flux Rope

### 2.1. HAWC Observatory

The High Altitude Water Cerenkov observatory is located on a plateau between the Sierra Negra and Pico de Orizaba volcanoes in Mexico, at 18°59′41″N, 97°18′30″.6W and at an altitude of 4100 m. HAWC consists of 300 water Cerenkov detectors (WCDs), each 7.3 m in diameter and 4.5 m deep. The WCDs are spread over an area of 22,000 m² and each one is filled with filtered water and instrumented with four photomultiplier tubes (PMTs). A 10 inch PMT is located at the center of the WCD and three 8 inch PMTs are arranged around it, making an equilateral triangle of side 3.2 m (Abeysekara & HAWC Collaboration 2012).

The main data acquisition (DAQ) system measures arrival times and time over threshold of PMT pulses. This information is used to reconstruct the air-shower front and estimate the arrival direction and energy of the primary particles. The electronics are based on time-to-digital converters (TDCs), and the main DAO also has a scaler system that counts the hits inside a time window of 30 ns for each PMT (R<sub>1</sub> rate from now on) and the coincidences of two, three, and four PMTs in each WCD, called multiplicity  $M_2$ ,  $M_3$ , and  $M_4$ , respectively. The TDC-scaler system allows one to measure particles with relatively low rigidity, from the cutoff rigidity at the HAWC site ( $\sim$ 8 GV) to the low limit of the reconstructed showers  $(\sim 100 \text{ GV})$ . The median energy of observation of the TDCscaler system and multiplicities are in the range of 40–46 GV. The large area and low cutoff rigidity of HAWC make it a suitable instrument for studying solar modulation in general and space weather in particular. Summarizing, we can say that the TDC-scaler rate used in this work provides information on the primary GCR flux above cutoff rigidity (from 8 GV onward) reaching Earth's atmosphere, which can be measured with high precision.

### 2.2. TDC-Scaler Data Reduction

During long periods of observation, the efficiency of PMTs may vary, so to carry out high-precision studies, it is necessary to correct for these drifts. To perform these corrections, first we have identified relatively stable PMTs during a year by continuously checking their deviations. Using a "singular value decomposition" method, we compute a reference rate that was used to model the slow and small changes in the efficiency of the remaining PMTs and correct for their variation in efficiency. Due to the large collecting area and high altitude of HAWC, the rate of observed particles is high: for instance, during the year 2016 the efficiency-corrected average rate of the HAWC TDC–scaler system was

 $\langle R_1 \rangle = 23.39 \,\text{kHz}$  per PMT; similarly for multiplicities the average rates per WCD were  $\langle M_2 \rangle = 8.06 \, \text{kHz}$ ,  $\langle M_3 \rangle = 5.69 \, \text{kHz}$ , and  $\langle M_4 \rangle = 4.35 \, \text{kHz}$ . The analysis carried out in this study is using data with "one minute" resolution, and for uniformity the rates were converted to percentage deviation with respect to the mean rate of the year 2016. It is worth mentioning that after the efficiency correction, the measured TDC-scaler rates are in agreement with the expected statistical accuracy of the data. Similar to other air-shower detectors, the TDC-scaler rates show a dependence on barometric pressure. We correct this pressure modulation following the method described by Arunbabu et al. (2019). Finally, due to HAWC's location near the equator and its lower cutoff rigidity of 8 GV, the solar diurnal anisotropy (DA) component is strongly significant in its low-energy observations. The DA was removed from the data using a band rejection filter that removes all the frequencies within the frequency range of  $\sim$ 1–2 cycles per day.

The efficiency-corrected TDC–scaler rates of all the PMTs were combined to provide the  $R_1$  rate with a statistical accuracy <0.01% per minute. The same efficiency correction process was also applied to the multiplicity rates from all the WCDs, and these were combined to get  $M_2$ ,  $M_3$ , and  $M_4$ .

#### 2.3. TDC-Scaler and Solar Modulation

The TDC-scaler data after applying all these corrections are shown in the top panels of Figures 2 and 3, where the mean values of the four channels  $R_1$  (blue),  $M_2$  (black),  $M_3$  (green), and  $M_4$  (red) are shown. The second and third panels of these figures show the solar wind (SW) proton measurements of the speed V (black), the number density N (green), the magnitude of the magnetic field B (black), and its components  $B_X$  (blue),  $B_Y$  (green), and  $B_Z$  (red). The one-minute resolution SW parameters were obtained from the OMNI data service developed and supported by NASA/Goddard's Space Physics Data Facility. The flow and magnetic pressures (fourth panel) as well as the  $D_{ST}$  index (bottom panel) were obtained from the World Data Center for Geomagnetism, Kyoto (Nose et al. 2015).

In order to show the suitability of the HAWC TDC-scaler system to study the solar modulation on short and medium timescales, Figure 2 shows a time period of approximately three months at the end of 2016, where seven HSSs (marked with yellow shadow areas) and one ICME and its MFR (blue shadow) were observed. From this figure the visible correlation of HAWC rates with the SW velocity resembles the advection effect of the GCRs in the heliosphere. Also the diffusion effects of GCRs inside the heliosphere show correlated decreases in HAWC rate with the magnetic field enhancements. It should be noted that, contrary to expectation, the signature of the MFR structure caused an increase in the rates, which is fairly remarkable (the aim of this analysis is to study the origin of this increase). In a similar way, the changes in the magnetic field, flux, and magnetic pressures and  $D_{\mathrm{ST}}$  index caused by this MFR are clearly distinguished from the other SW structures detected over this period.

<sup>&</sup>lt;sup>29</sup> The OMNI data set with one-minute resolution is created from in situ measurements by ACE, Wind, and DSCOVR (King & Papitashvili 2005). These spacecraft are located at the L1 point.

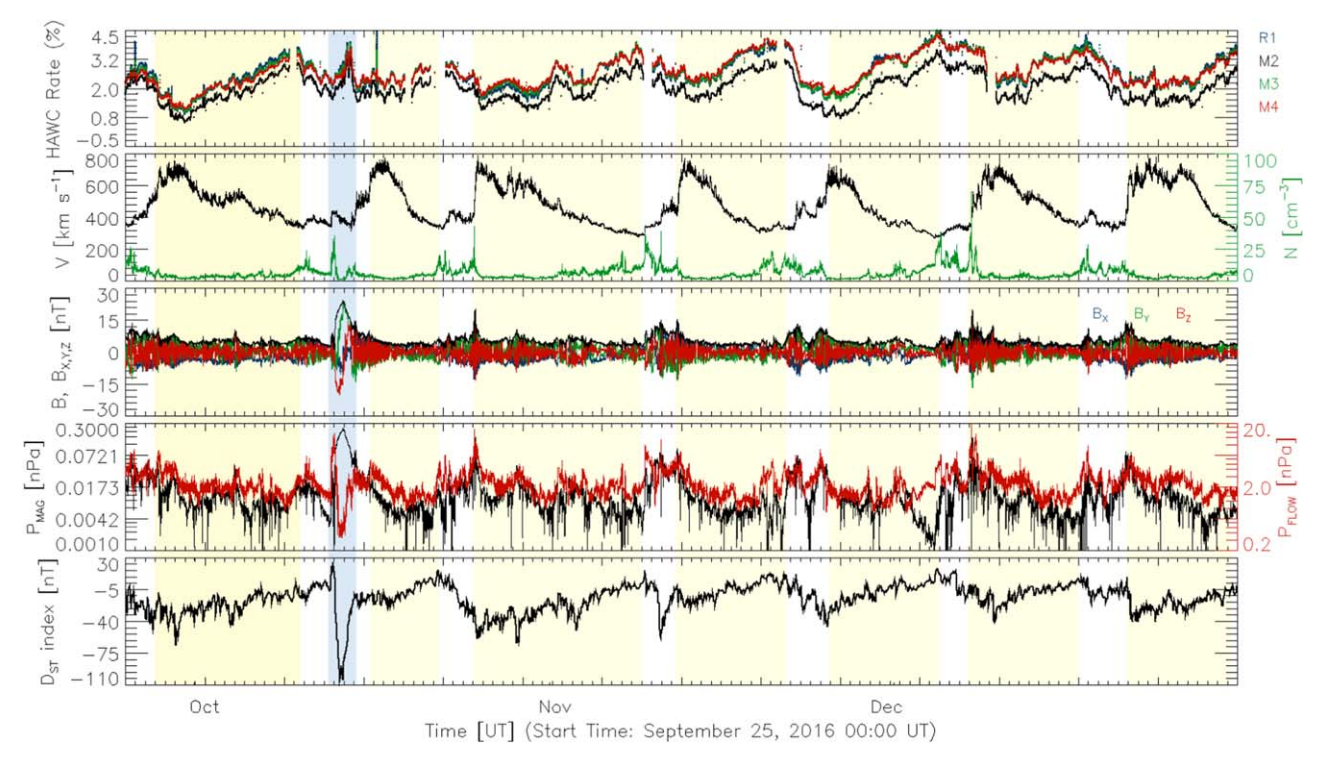


Figure 2. From top to bottom: HAWC TDC-scaler rates ( $R_1$ ,  $M_2$ ,  $M_3$ , and  $M_4$ ; blue, black, green and red, respectively); from the OMNI data, the SW measurements of the speed V and the number density N (both shown in the second panel by black and green solid lines); the components ( $B_X$ ,  $B_Y$ , and  $B_Z$ ) and magnitude of the B-field (shown in the third panel and colored blue, green, red, and black, respectively); the magnetic and flow pressures (black and red lines in the fourth panel), and the  $D_{ST}$  index (bottom panel) from the World Data Center for Geomagnetism, Kyoto, for the period of time between 2016 September 25 and 2016 December 31. The yellow shaded areas show the periods of time within HSSs, whereas the blue shading marks the MFR time. The narrow peaks seen in the TDC-scaler rates on October 1 and 16 are due to atmospheric electric field disturbances.

### 2.4. TDC-Scaler Rates during the MFR Passage

The GCR modulation associated with the ICME passage during 2016 October observed by HAWC can be seen in Figure 3 (see Section 3.3 for the details of the figure panels). During this time, the TDC–scaler rates increased as a double peak structure, starting around 02:50 UT on 2016 October 14 and lasting 16.8 hr.

The HAWC TDC-scaler rates have a background rate of  $4.25 \times 10^8$  particles per minute. During this event, the integrated counts had an excess of  $1.76 \times 10^9$  particles above the background level. In order to quantify the noise level of the TDC-scaler system, we computed the mean rates and standard deviation of the 1200 PMT rates for  $R_1$  and 300 WCD rates for multiplicities  $M_2$ ,  $M_3$ , and  $M_4$  every minute. The upper panels of Figure 4 show the distributions of the computed standard deviations during three days of our period of interest. The mean values of these distributions are used as the standard deviation of the observations  $(\sigma)$  for this study and are listed in the second column of Table 1. The magnitude of the observed double peak structure as a percentage is estimated as the difference between the peak and pre-event intensities and is shown in the third and fifth columns of Table 1. In a similar way, the magnitude in terms of standard deviation ( $\sigma$ ), i.e., magnitude  $/\sigma$ , which we call the significance of the increase, is shown in the fourth and sixth columns.

It should be noted that during the event, the weather at the HAWC site was calm and no electric field disturbances were recorded by the site electric field monitor. The atmospheric pressure at the site was also showing normal behavior, which rules out the possibility of abnormal atmospheric activities. Earthquakes can also cause rate increases in the TDC–scaler

system but these last a few minutes and there is no report of an earthquake of magnitude greater than 5.5 during our period of interest in the south-central part of Mexico, where HAWC is sited.

To compare this event with other short-term modulations observed by the TDC-scaler system, we applied a high-pass filter to the rates. This filter removed all the frequencies smaller than 1 day<sup>-1</sup> and retained all the fast variations in the data that have timescales less than a day. The bottom panel of Figure 4 shows the high-pass-filtered data during three months, starting on 2016 September 1. The standard deviation of this high-passfiltered data for the entire year 2016 was estimated as  $\sigma_{\text{high-pass}} = 0.068\%$ . From the figure it is clear that the MFR event (marked by the blue shaded area) is significant in comparison to all other short-period modulations, and is much higher than the  $5\sigma_{high-pass}$  level. In this figure one can also see atmospheric electric field transients (short-time spikes of tens of minutes). In contrast, the event due to the MFR lasted  $\sim$ 17 hr. These atmospheric electric field events are listed in Jara Jimenez et al. (2019) except for those on September 21 and 26; these two days were not listed due to short gaps in HAWC TDC-scaler data.

# 3. Magnetic Flux-rope Origin, Transport, and Geomagnetic Effects

### 3.1. The Quiet Filament Eruption

On 2016 October 8 a filament was observed by the Atmospheric Imaging Assembly (AIA, Lemen et al. 2012) on board the Solar Dynamics Observatory (SDO, Pesnell et al. 2012) activated at  $\sim$ 04:00 UT in the northeast quadrant

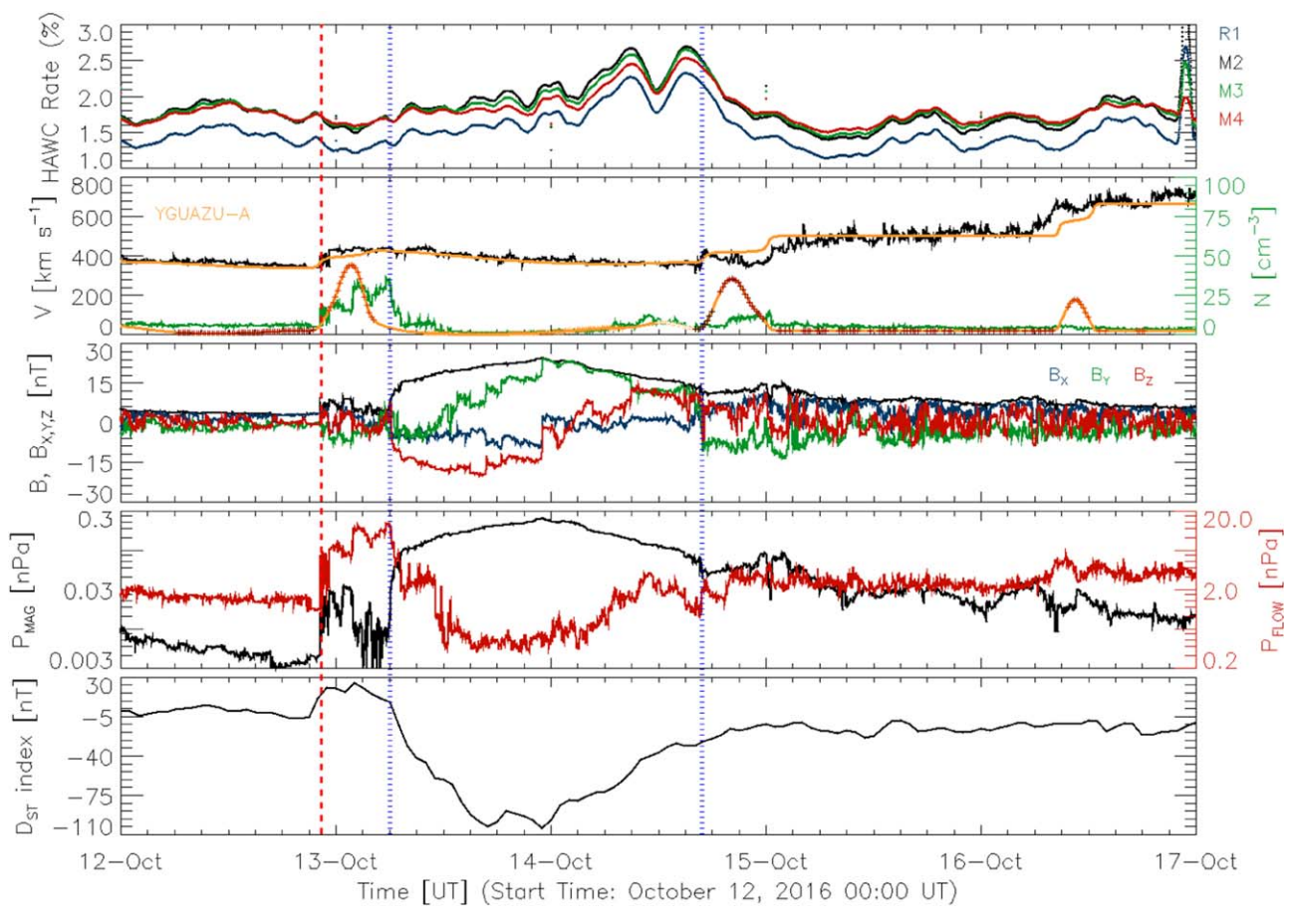


Figure 3. The MFR observed in the interplanetary medium, the associated geomagnetic storm, and its effects on the GCR flux. From top to bottom: GCR rates measured by the HAWC TDC-scaler system (the PMT and multiplicity rates are marked with different colors, see Section 2 for their definitions); speed V (shown in black) and number density N (green); the components  $(B_X, B_Y, \text{ and } B_Z, \text{ colored blue, green, and red, respectively)}$  and magnitude of the magnetic field B (black); the magnetic (black) and flow (red) pressures; and the  $D_{ST}$  (disturbance storm-time) index (black). The SW parameters are extracted from the OMNI data (King & Papitashvili 2005), and  $D_{ST}$  from the World Data Center for Geomagnetism, Kyoto (Nose et al. 2015). In the second panel, we overlapped in orange, the synthetic profiles of N and V obtained with YGUAZÚ-A code (the simulation is described in Section 3.4). The code enables us to tag and follow different plasma parcels marked in the synthetic number density profile with colored symbols as described in Table 2. The dashed vertical red line marks the shock and the two dotted blue lines mark the start and end times of the slow CME constraining an MFR. The increase in TDC-scaler rate observed at October 16 at  $\sim$ 23 UT was caused by an atmospheric electric field transient and is unrelated to this investigation (Lara et al. 2017; Jara Jimenez et al. 2019).

(see panels (a) and (b) of Figure 5), rising with a speed of  $\sim 20 \text{ km s}^{-1}$  during the next 20 hr. Around 00:00 UT on 2016 October 9 and at an altitude of  $\sim 3 R_{\odot}$  an acceleration process started as seen by COR1 and COR2, instruments on board the Solar Terrestrial Relations Observatory (STEREO, Kaiser et al. 2008) spacecraft (green and red X symbols, respectively, in panel (e) of Figure 5), and reached a speed of  $\sim 180 \text{ km s}^{-1}$ .

The filament was part of a halo CME observed on 2016 October 9 at 02:45 UT by the Large Angle and Spectrometric Coronagraph (LASCO) on board the Solar & Heliospheric Observatory (SOHO). This eruption was seen as a limb CME, showing a dark cavity surrounded by bright material (typical structure of the cross section of an MFR, e.g., Dere et al. 1999) by the Sun Earth Connection Coronal and Heliospheric Investigation (SECCHI) on board the STEREO A spacecraft (panels (c) and (f) of Figure 5, respectively).

## 3.2. The Magnetic Flux-rope Transport in the Interplanetary Medium

The ICME propagation from the Sun to the Earth of the 2016 October event has been studied previously by He et al. (2018),

who combined remote sensing observations from SDO, STEREO, and SOHO and in situ measurements as extracted from OMNI data. These authors focused their work on understanding the geo-effectiveness associated with the CME magnetic field structure. They reconstructed the CME using the Grad-Shafranov technique to identify the MFR with a strong southward magnetic field, which produced the geomagnetic storm (see Figure 8 of He et al. 2018). They also simulated the SW with the ENLIL-MHD code (Odstrcil et al. 2004) to illustrate the background SW conditions during the ICME propagation. However, they only considered the evolution of the ICME bracketed between two HSSs, without considering that the whole of this system is propagating within a variable SW. We note that in the case of slow CMEs the Sun-Earth travel time may be a few days and therefore they have the opportunity to interact with other SW structures and/or transients that can enhance or ensure their geo-effectiveness (e.g., He et al. 2018; Chen et al. 2019).

To include this ingredient in the scenario (a variable ambient SW), we perform a simulation that includes the observed parcels of SW with different speeds and densities, including the slow ICME and the slow and fast flows (Section 3.4).

## Distribution of standard deviation of HAWC TDC-scaler rate

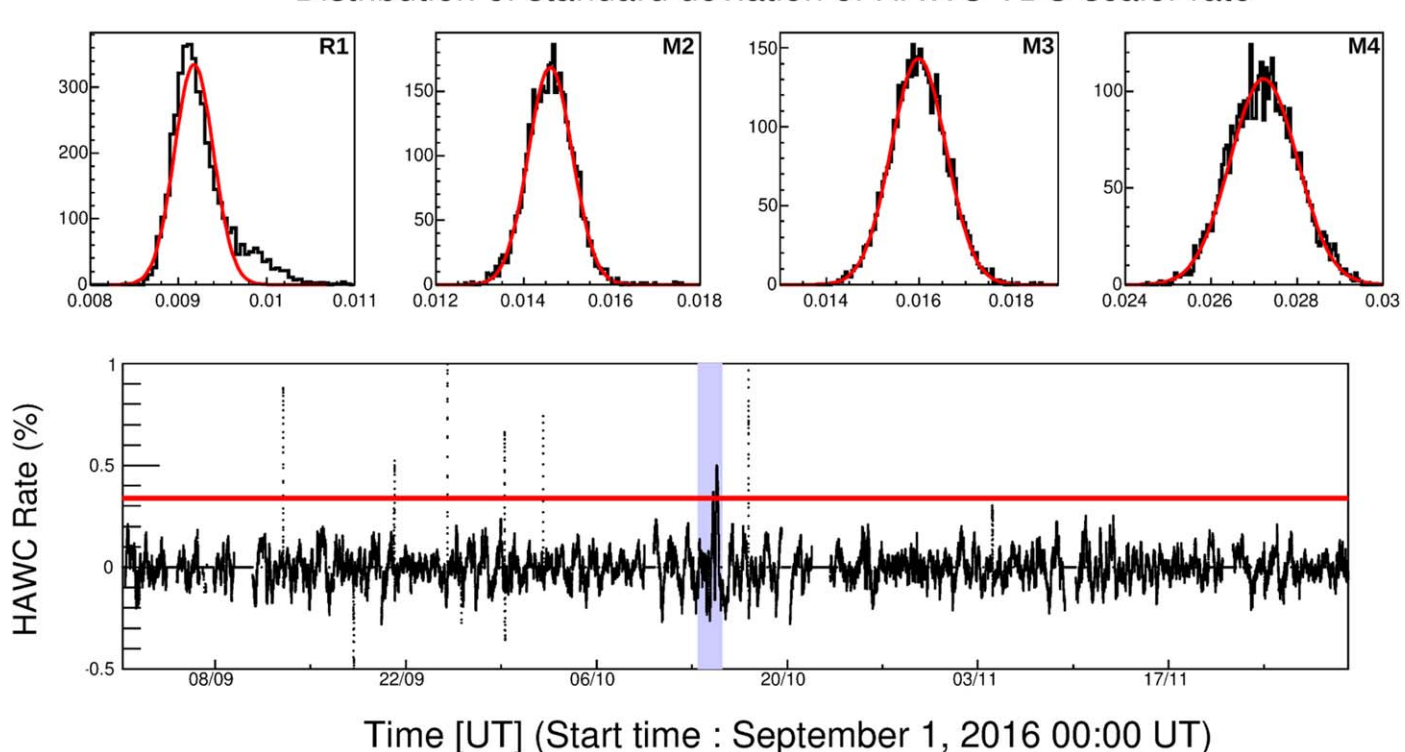


**Figure 4.** The upper panels show the distributions of 1 minute standard deviation of the HAWC TDC–scaler rates. The distributions cover observations over a period of three days: 2016 October 13–15. The bottom panel shows the HAWC TDC–scaler rate  $R_1$  after applying a high-pass filter; with a cutoff frequency of 1 day<sup>-1</sup>. The red line shows the limit of five times standard deviation of this high-pass-filtered data, and the blue shaded region marks the period of time when the MFR was observed.

Table 1
Magnitude of the Double Peak Structure

| TDC-<br>scaler                                              | σ                                                                                       | Magnitu                              | de of Peak 1                 | Magnitude of Peak 2                  |                              |  |
|-------------------------------------------------------------|-----------------------------------------------------------------------------------------|--------------------------------------|------------------------------|--------------------------------------|------------------------------|--|
|                                                             | (%)                                                                                     | (%)                                  | in Terms of $\sigma$         | (%)                                  | in Terms of $\sigma$         |  |
| R <sub>1</sub> M <sub>2</sub> M <sub>3</sub> M <sub>4</sub> | $9.18 \times 10^{-3}$ $1.46 \times 10^{-2}$ $1.60 \times 10^{-2}$ $2.72 \times 10^{-2}$ | 0.7122<br>0.7562<br>0.7235<br>0.6690 | 77.6<br>51.8<br>45.2<br>24.6 | 0.7761<br>0.7843<br>0.7940<br>0.7570 | 84.6<br>53.7<br>49.7<br>27.8 |  |

**Note.** The magnitudes in terms of percentage deviation (difference between the peak and pre-event intensities) of the first and second peaks within the double peak structure as observed in the HAWC TDC-scaler rate  $(R_1)$  and multiplicities  $(M_2, M_3,$  and  $M_4)$  are given in the third and fifth columns. The standard deviation during the observation  $(\sigma)$  of the TDC-scaler rate is shown in the second column, and the significance of the increases or magnitudes in terms of  $\sigma$  is given in the fourth and sixth columns.

### 3.3. In Situ Observation of the ICME

When an interplanetary transient is not fast enough, it may still be able to modulate the GCR flux depending on its magnetic field strength and geometry, its dynamics compared with ambient SW, and its interaction with the Earth's magnetic field. This means that, in general, the GCR modulation depends mainly on three factors: the nature of the transient and its intrinsic magnetic field, the resulting conditions after the transient interacts with the ambient SW, and the Earth's magnetosphere.

During 2016 October 12–17, a slow ICME was identified at 1 au using the one-minute resolution in situ measurements (this event has been reported by Nitta & Mulligan 2017; He et al. 2018).

At this time, the TDC-scaler subsystem of the HAWC observed a peculiar GCR flux modulation in the form of a double peak enhancement as shown in the top panel of Figure 3, where HAWC TDC-scaler data— $R_1$ ,  $M_2$ ,  $M_3$ , and  $M_4$ —are presented. This figure also shows the SW parameters: V, N (second panel), B-field (third panel), the flow and magnetic pressure (fourth panel), as well as the  $D_{ST}$  index (bottom panel). We have marked with a dashed vertical red line the arrival time of the shock at 1 au, whereas the two dotted vertical blue lines mark the starting and ending times of the CME structure at 1 au as discussed by Nitta & Mulligan (2017) and He et al. (2018). The ICME boundaries were selected based on the signatures described on Zurbuchen & Richardson (2006) and Richardson & Cane (2010). There is a shock wave on 2016 October 12 at 22:01 UT and a sheath that lasted for 7.68 hr. The MFR boundaries are very well defined with the magnetic field and plasma parameters, starting on 2016 October 13 at 06:00 UT and ending on 2016 October 14 at 16:00 UT with a bulk speed of  $390 \,\mathrm{km \, s^{-1}}$ .

Due to the well-defined magnetic structure with clear rotation of  $B_Y$  and  $B_Z$  (in situ measurements), the slow CME has been identified as an MC or MFR with a strong southward magnetic field (He et al. 2018). As stated above, this MFR was the result of the expulsion of a quiet filament with no obvious eruptive signatures in remote sensing observations (Nitta & Mulligan 2017). At 1 au, the conditions that give rise to the increase in GCRs started with a pre-event

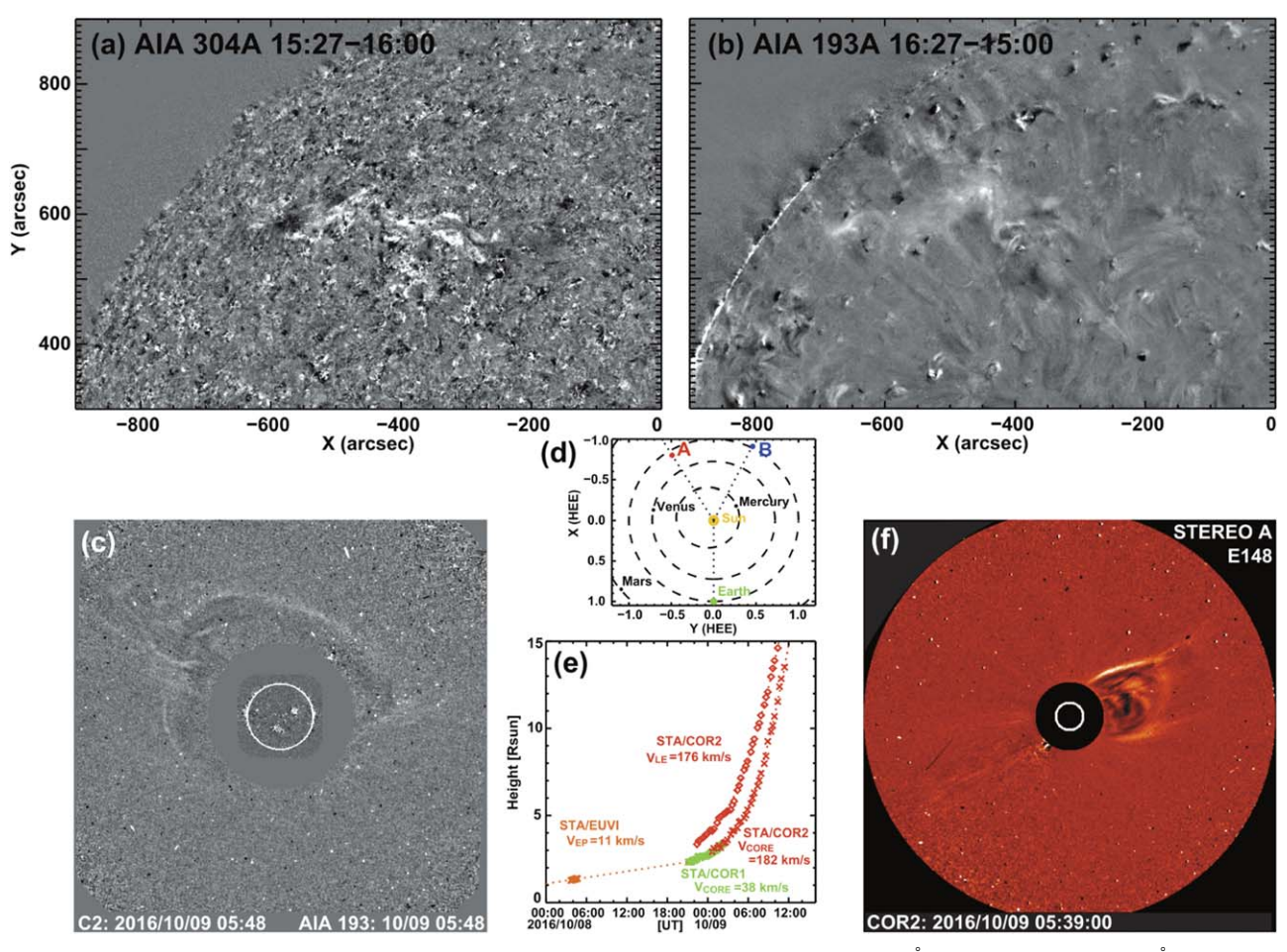


**Figure 5.** Two stages of the 2016 October 8 filament eruption seen in the *running differences* images of AIA 304 Å at 15:27 UT and AIA 193 Å at 16:27 UT (white and black continuous areas at the center of panels (a) and (b), respectively). The associated halo and limb CME seen by LASCO (aboard the SOHO spacecraft) and SECCHI (aboard the STEREO A spacecraft) are shown in panels (c) and (f), respectively. The relative positions of the spacecraft in interplanetary space are shown in panel (d), where SOHO and Wind are close to the Earth (marked in green) and the positions of STEREO A and B are marked in red and blue respectively. The height-time diagrams associated with the evolution of the filament (orange crosses) and CME leading edge (red diamonds) and core (green and red crosses) are plotted in panel (e).

HSS (October 1) sweeping the interplanetary medium and imposing very quiet SW conditions ( $V \sim 350 \, \mathrm{km \, s^{-1}}$  and  $N \sim 7$  particles cm<sup>-3</sup>) in front of the ICME. This smooth SW coupled with the low ICME speed ( $\sim$ 450 km s<sup>-1</sup>) led to a weak shock and small compression region (sheath, marked with red and blue vertical lines around October 13 in Figure 3). The magnetic pressure  $(P_{\text{MAG}}(\text{nPa}) = (10^{-2}/8\pi)B(\text{nT})^2$ , black) and the SW flow pressure (computed  $P_{\text{FLOW}}(\text{nPa}) = 2 \times 10^{-6} N(\text{particles cm}^{-3}) V(\text{km s}^{-1})^2,$ are shown in the fourth panel of Figure 3, to make it clear that this slow ICME is related to a strong magnetic field disturbance. It can be seen that within the MFR (between the two dotted vertical blue lines),  $P_{\rm MAG}$  increases while  $P_{\rm FLOW}$ decreases, both considerably in comparison to the pressure conditions before the arrival of the MFR (i.e., before the dashed vertical red line). Moreover, the MFR arrival at the Earth produced a relatively intense geomagnetic storm reaching a minimum  $D_{\rm ST}$  index of  $\sim -104$  nT (He et al. 2018) as shown in the bottom panel of Figure 3.

## 3.4. Simulations of the ICME Transport and Surrounding Solar Wind Conditions

It is important to note that during 2016 October solar activity was in the declining phase of Cycle 24, therefore the SW

conditions that we simulate correspond to an interval of low activity in the inner heliosphere. As the CME propagates 3° east of the Sun–Earth line and 11° north of the ecliptic plane (for further information see Figure 2 and its description from He et al. 2018), we assume that it propagates radially and is directed toward the Earth, and therefore we neglect the deflection and rotation effects (Kay & Opher 2015) as well as its interaction with the SW magnetic field (Schwenn et al. 2005). Under these assumptions, hydrodynamic codes give reliable insights into the dynamics of CMEs in the SW (Niembro et al. 2019).

The simulation was done using the 2D hydrodynamic, adiabatic, and adaptive grid code YGUAZÚ-A, developed by Raga et al. (2000) and used previously to simulate the propagation of ICMEs in the SW (see Niembro et al. 2019, for the details of the code and its application to ICMEs). We assume a standard SW (e.g., Kippenhahn et al. 2012) with a mean molecular weight<sup>30</sup>  $\mu = 0.62$  to consider a chemical composition with solar mass fractions of 0.7 H, 0.28 He, and 0.02 of the rest of the elements; a specific heat at constant

<sup>&</sup>lt;sup>30</sup> The mean molecular weight refers to the average mass per particle in units of the mass of a hydrogen atom.

| At 1 au (from OMNI data) |                  |                   |     |       |      |       | Near the Sun (from Cantó et al. 2005) |  |
|--------------------------|------------------|-------------------|-----|-------|------|-------|---------------------------------------|--|
|                          |                  |                   |     |       |      |       |                                       |  |
| A                        | 2016/10/12 00:00 | 2016/10/12 11:55  | 372 | 5.86  | 2.78 | b     | 363                                   |  |
| В                        | 2016/10/12 20:35 | 2016/10/12 22:15  | 340 | 4.82  | 1.23 | 29.32 | 330                                   |  |
| C                        | 2016/10/12 23:18 | 2016/10/13 11:08  | 431 | 17.4  | 5.61 | 11.83 | 423                                   |  |
| D                        | 2016/10/14 08:48 | 2016/10/14 16:08  | 360 | 7.49  | 2.02 | 16.5  | 351                                   |  |
| E                        | 2016/10/14 16:53 | 2016/10/14 18:33  | 405 | 5.53  | 1.68 | 1.66  | 397                                   |  |
| F                        | 2016/10/14 21:33 | 2016/10/14 23:23  | 358 | 10.96 | 2.94 | 16.79 | 349                                   |  |
| G                        | 2016/10/15 01:03 | 2016/10/16 06:30  | 502 | 4.51  | 1.69 | 66.71 | 495                                   |  |
| Н                        | 2016/10/16 08:43 | 2016/10/16 17:03  | 665 | 3.87  | 1.93 | 44.05 | 660                                   |  |
| I                        | 2016/10/16 18:58 | 2016/10/18 04:18° | 705 | 2.32  | 2.25 | 56.38 | 700                                   |  |

**Notes.** The values are extracted from the OMNI data set and the computed mass-loss rate  $\dot{M}$  used to reconstruct the SW conditions ( $V_{\rm inj}$ ,  $\Delta t$ ) near the Sun at the injection radius  $R_{\rm inj} = 6~R_{\odot}$  obtained by solving the system of equations described in Cantó et al. (2005). We have tagged with different colors the periods to be identified and followed in Figures 3 and 6.

period B.

volume of  $\gamma = 5/3$ , and an initial temperature of  $10^5$  K (Wilson et al. 2018).

The SW conditions at the injection radius  $R_{\rm inj}=6~R_{\odot}$  (4.2 × 10<sup>6</sup> km, ~0.028 au) were estimated by splitting the SW measurements at 1 au into different time periods i=A, B, C, ..., I, in which the SW showed a speed with a relatively stationary behavior. With this, we estimated the median values of the speed  $\overline{V_{\rm l}}_{\rm au_i}$  and the number density  $\overline{N_{\rm l}}_{\rm au_i}$ . Each period is characterized with these median values. Then, we computed the mass-loss rate as  $\dot{M_i}=4\mu m_p\pi R_{\rm l}^2$  au  $N_{\rm l}$  au,  $V_{\rm l}$  with the proton mass  $m_p=1.67\times 10^{-27}~{\rm kg}$ . With all these parameters obtained from the measurements at 1 au, we obtained the speed  $V_{\rm inj_i}$  at the injection point  $R_{\rm inj}$  (near the Sun) and injection time  $\Delta t_i$  by solving the system of equations described in Cantó et al. (2005). All these values are shown in Table 2, with the MFR corresponding to period C. The computational domain is

filled with the conditions described in period A (corresponding

to the ambient SW conditions) and the initial injection time is

given by the model using the SW speed observed within

The synthetic speed and number density profiles resulting from the simulation are shown as orange solid lines in the second panel of Figure 3 to be compared with the in situ measurements at 1 au (shown in the figure in black and green, respectively). It can be noticed that our approach accurately resembles the observed speed profile, while the number density profile is consistent with the observations, except for those time ranges in which the 3D configuration of the magnetic field certainly plays a major role in the dynamics (e.g., Cargill & Schmidt 2002), such as in the compression region formed due to the interaction of the MFR with the ambient SW in front of it and delimited by the dashed red vertical line (shock) and the first dotted blue vertical line (initial time of the MFR). The other two enhancements found at later times in the number density profile (2016 October 14 ~17:00 UT and 2016 October  $16 \sim 12:00$  UT) are related to compression regions formed by the interaction between two flows at different speeds (between periods F and G, and G and H, respectively). It is worth noting that, from the hydrodynamics point of view, the plasma is compressed when two flows at different speeds interact, while a low-density region will be formed when the flows separate from each other,.

An important feature of this particular hydrodynamic code is that it enables us to tag and follow each different plasma parcel. This is shown with the colored symbols used over the synthetic number density profile, which are indicated in Figure 3 following the slightly lighter color code in Table 2. We would like to focus on the evolution of two of the simulated SW parcels colored green (corresponding to period B) and orange (period D). It can be noticed that the SW delimited in these two periods presents low-density cavities that can be easily tracked in Figure 6, where we show the profiles of speed (black solid line) and number density (green solid line with colored symbols) at five different heliospheric distances: 0.1 au, 0.3 au, 0.5 au, 0.7 au, and 1.0 au, from top to bottom.

These low-density cavities prevented the interaction of the disturbance with the surrounding ambient SW, preserving the well-defined and strong magnetic structure of the MFR from its source up to 1 au. Moreover, the duration of the CME (48 hr, time delimited by dashed blue lines in Figure 3 and blue shaded area in Figure 6) does not change at different heliospheric distances, thus allowing the guiding of GCRs observed by HAWC.

## 3.5. Effects of the Magnetic Flux Rope on the Earth's Magnetospheric Field

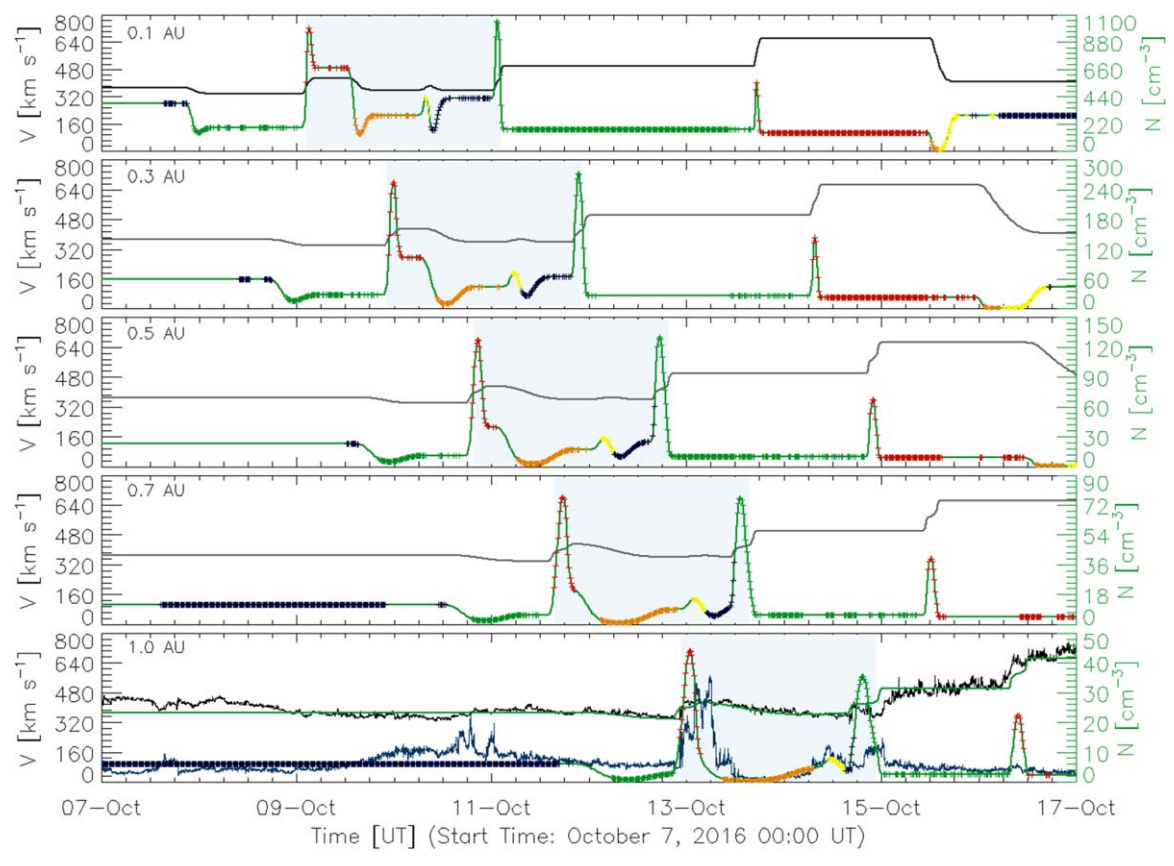
Besides the spacecraft located around the L1 point, there are several spacecraft orbiting the Earth at different locations that are able to detect changes in the Earth's magnetic field caused by the ICME (shock, sheath, and flux rope) as it arrives in the Earth's vicinity. In this work, we use *B*-field data from THEMIS-E and THEMIS-C (Angelopoulos 2008), GOES-15 (https://www.goes.noaa.gov/goesfull.html), and MMS-1 (Burch et al. 2016) to characterize the disturbances caused by the 2016 October MFR on the Earth's magnetosphere and its possible effects on the GCR flux.

Figure 7 shows the orbits of these spacecraft in the XY (left) and XZ (right) GSE planes (the geocentric GSE is a right-handed

a (yyyy/mm/dd hh:mm UT.)

b Period A corresponds to the SW conditions needed to fill in the computational domain in which the different periods will be injected.

<sup>&</sup>lt;sup>c</sup> The end of the period is not shown in Figures 3 and 6.



**Figure 6.** The synthetic profiles of speed (black solid line) and number density (green solid line) obtained by simulating the variable SW conditions with YGUAZÚ-A at five different heliospheric distances (from top to bottom): 0.1, 0.3, 0.5, 0.7, and 1.0 au. The colored symbols tag the different plasma parcels as listed in Table 2. The duration of the CME (48 hr delimited by the two maxima density enhancements shown in red and green respectively) is marked within a blue shaded area in each panel to show that it does not change during the evolution. The density cavities prevented the interaction of the CME with the surrounding SW, preserving its structure. In the bottom panel we show the comparison between the observed and synthetic SW speed (black and green lines respectively) and number density (blue and green lines respectively) at 1 au.

coordinate system with the X-axis pointing toward the Sun and the Z-axis perpendicular to the ecliptic plane and positive pointing north). The triangles on the panels in Figure 7 mark the spacecraft locations at the time when the magnetic field discontinuity associated with the arrival of the ICME-driven shock was observed (column 3 in Table 3 and vertical gray lines in the top panels of Figures 15–19 in Appendix A). The squares in Figure 7 mark the location of the sudden decrease in  $B_Z$ associated with the arrival of the leading edge of the MFR at each spacecraft (column 6 in Table 3). The bow shock boundary drawn (continuous line) was calculated from a modified version of Fairfield (1971), while the location of the magnetopause (dashed line) is based on the model of Roelof & Sibeck (1993); both boundaries are shown in Figure 7 only as a reference and are based on the SW average value of  $P_{\rm FLOW}=1.65~{\rm nPa}$ measured at 1 au. It is important to note that during the MFR passage these boundaries may be largely modified. According to this and in agreement with the observations, GOES-15, THEMIS-E, and MMS-1 were located inside the magnetosphere during the time interval studied, whereas THEMIS-C was in the magnetosheath region.

In general, inside the magnetosphere the magnetic field is dominated by the north-south geomagnetic dipole, i.e.,  $B_Z$  component. Therefore, we follow and compare the values of this B-field at different locations around the Earth during the MFR passage. In Figure 8, we show the difference  $|B| - B_Z$  normalized to the maximum value of |B| observed by

GOES-15, which, of the spacecraft considered in this work, was the one with the shortest and constant distance to the Earth at the time of the sudden decrease in  $B_Z$ . This difference was computed for all the spacecraft (plotted with different colors) during 2016 October 12, 13, and 14 (top, middle, and bottom panels of Figure 8 respectively). The data are in GSE coordinates except for GOES-15, which are presented in EPN (earthward, parallel, normal) coordinates with respect to the spacecraft's orbital plane (see Appendix A). The individual plots of the B-field and its components measured by each spacecraft during the event are shown in Figures 15–19 in Appendix A.

In Table 3, we summarize the times at which the spacecraft observed the shock-associated discontinuity of the B-field and their corresponding upstream/downstream B-values (columns 3, 4, and 5, respectively), the times of the sudden decrements of  $B_Z$  associated with the MFR and its minimum value (columns 6 and 7) as well as the magnetospheric location (column 8) of each analyzed spacecraft (column 2). The Geo projections of the spacecraft during the MFR passage are plotted in Figure 9.

As the MFR enters the magnetospheric region, following the ICME sheath region, the decrease in  $P_{\rm FLOW}$  (see fourth panel in Figure 3) associated with the internal region of the MFR produced an expansion of the Earth's magnetic field. This effect can be seen by comparing the October 13 time intervals 04:00–08:00 UT in Figure 16, 04:00–09:00 UT in Figure 17, and 08:00–10:00 UT in Figure 18 in Appendix A with the same

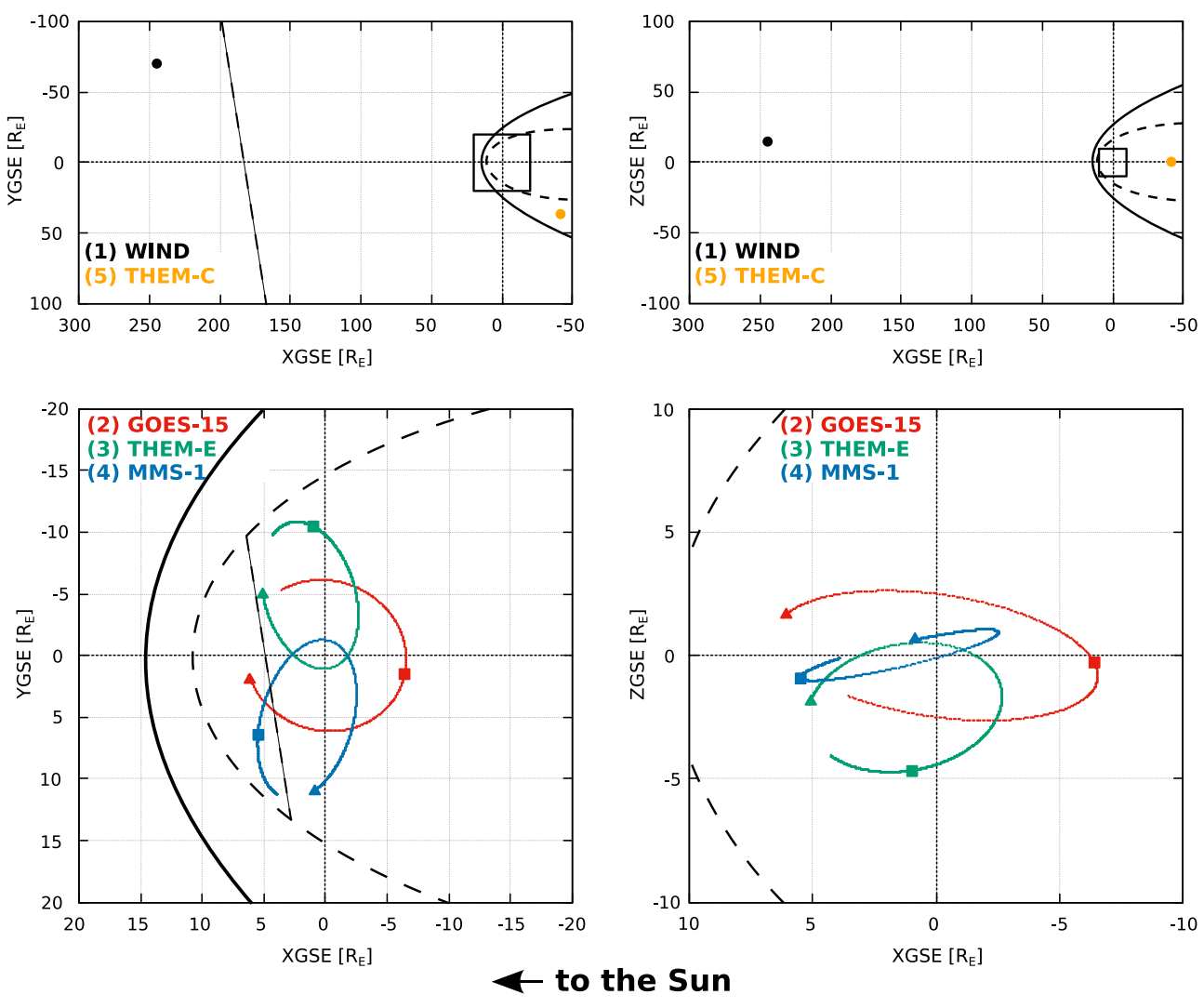


Figure 7. Spacecraft orbits/positions showing the shock/B-discontinuity time (triangle) and  $B_Z$  decrements (square) projected on XY (left) and XZ (right) GSE planes (where  $R_E = 6357$  km is the Earth's radius at the equator). The small square in each upper panel represents the area plotted in each lower panel. The number in brackets next to the spacecraft name indicates the timing of the shock/B-discontinuity observation. A model of the bow shock (continuous line) and magnetopause (dashed line) is shown. The  $9^{\circ}$  inclined dashed line in the XY panels corresponds to the orientation of the MFR major axis.

Table 3
Parameters Related to the Spacecraft Observations

| s/d | Spacecraft | t <sub>s/d</sub> (UT)<br>mm/dd hh:mm:ss | B <sub>up</sub> (nT) | B <sub>down</sub> (nT) | t <sub>BZ</sub><br>mm/dd hh:mm:ss | $\min(B_Z)$ (nT) | Spacecraft<br>Region <sup>a</sup> |
|-----|------------|-----------------------------------------|----------------------|------------------------|-----------------------------------|------------------|-----------------------------------|
| s   | WIND       | 10/12 21:15:37                          | 3.4                  | 8.2                    | 10/13 05:27:30                    | -20.0            | SW                                |
| d   | GOES-15    | 10/12 22:11:51                          | 121                  | 150                    | 10/13 08:00:00                    | 8.0              | M-SPH                             |
| d   | THEMIS-E   | 10/12 22:13:33                          | 92.5                 | 123                    | 10/13 10:19:21                    | -60.0            | M-SPH                             |
| d   | MMS-1      | 10/12 22:13:52                          | 30                   | 47                     | 10/13 10:31:10                    | -50.0            | M-SPH                             |
| S   | THEMIS-C   | 10/12 22:24:49                          | 6                    | 10.5                   | 10/13 06:31:37                    | -22.5            | M-SH                              |

#### Note.

time period during the previous day. This effect is clearer for GOES-15 in Figure 16 due to its geostationary orbit.

This magnetospheric weakening, along with the enhancement of the southward magnetic field component inside the MFR, caused sudden reversals ( $B_Z < 0$ ) on the Earth's magnetic field observed as step-like signatures by THEMIS-C, THEMIS-E, and MMS-1 as shown in the middle panel of

Figure 8, and as changes in the polarity of  $B_Z$  in Figures 17–19 in Appendix A.

Because of the unique position of GOES-15, particularly its proximity to the ecliptic plane and its low altitude, the intense local magnetic field makes it difficult to clearly detect the perturbation caused by the MFR, as shown in Figure 8 and in Figure 16 in Appendix A. However, significant disturbances

a s/d: shock or discontinuity, SW: solar wind, up: upstream, down: downstream, M-SPH: magnetosphere, M-SH: magnetosheath.

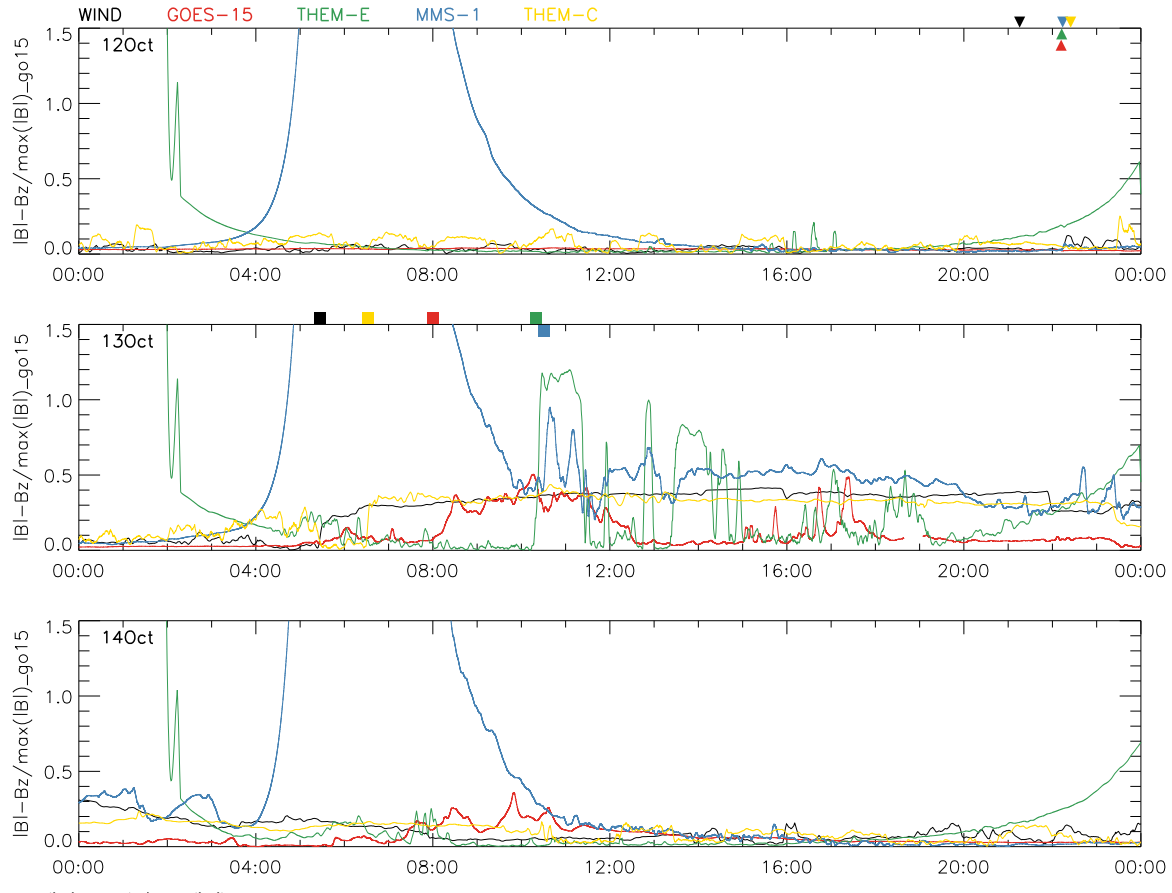
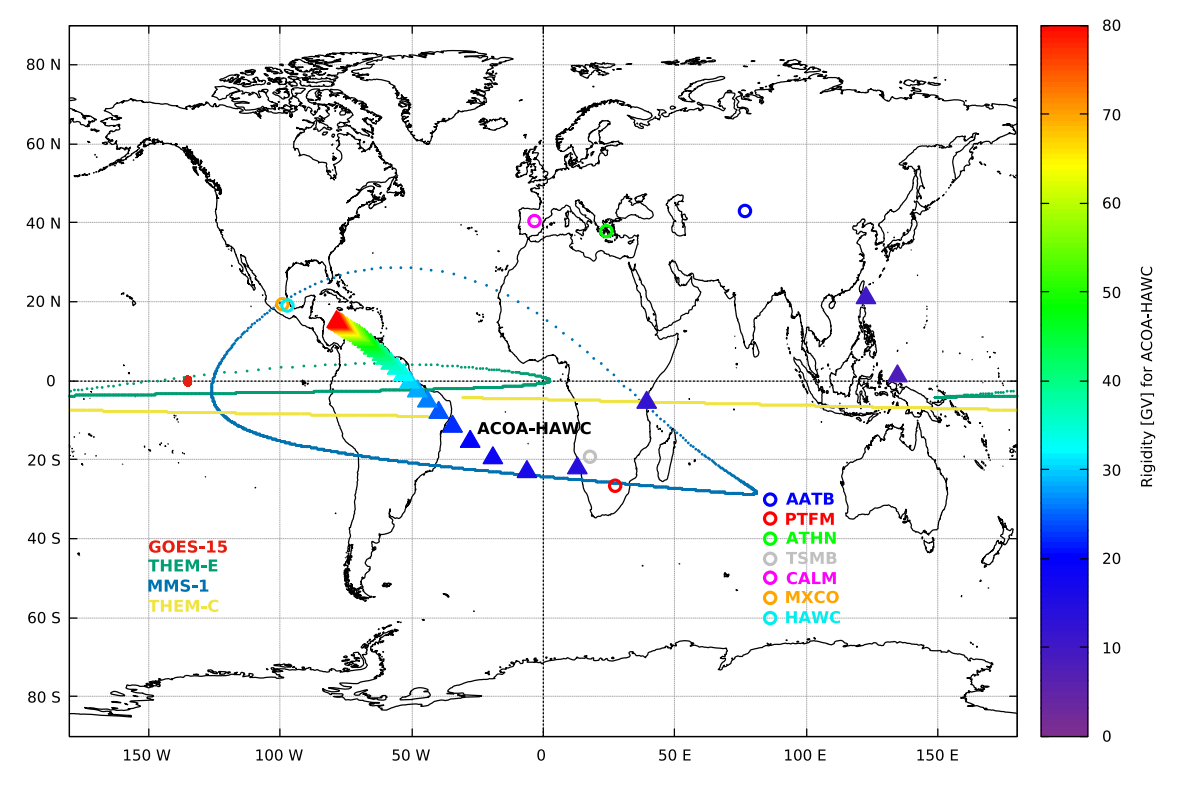
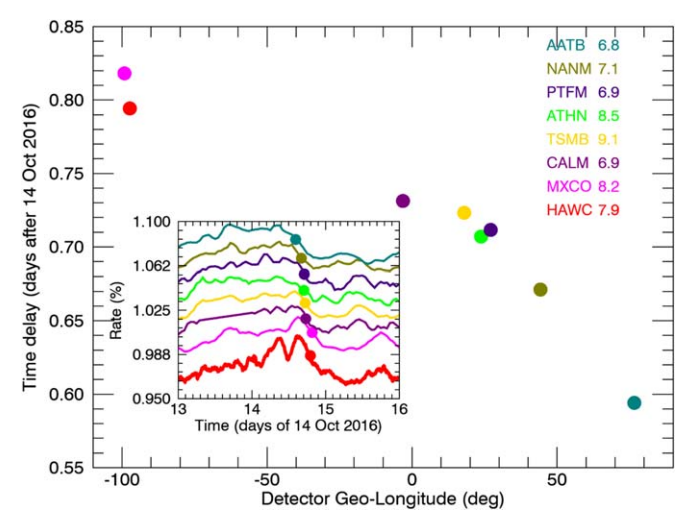


Figure 8. Plot of  $(|B| - B_Z) / \max(|B|)_{GOES-15}$  for all the spacecraft (in different colors) observed on 2016 October 12 (top), 13 (middle), and 14 (bottom). The colored symbols in panels correspond to the timing of the *B*-discontinuity (triangles) and  $B_Z$  decrement (squares) according to Table 3 and Figure 7.



**Figure 9.** Geo projection of spacecraft paths (continuous and dotted lines) corresponding to 2016 October 13 and location of neutron monitors (open colored circles). The rainbow-triangle-path crossing the equator line indicates the rigidity values (shown in the color palette) for the asymptotic cone of acceptance for the HAWC observatory (marked as ACOA-HAWC).



**Figure 10.** The MFR passage observed by different NMs around the world, whose cutoff rigidities (in GV) are similar to those of HAWC (the acronym and cutoff rigidity of each monitor is in the upper right corner). The main plot shows the delay of the decrease in perturbation as a function of the Geolongitude of each NM. The inset shows the time profiles of the NMs as well as the  $M_3$  HAWC rate divided by 30.

were observed during most of October 13 and continued but with lower amplitude the next day, when the GCR double peak was observed by HAWC. This can be corroborated by observing the middle and bottom panels in Figure 8, showing in this way that the GCR enhancement observed by HAWC was not directly caused by these geomagnetic disturbances.

# 3.6. Ground-level Observations by HAWC and Neutron Monitors

Although the GCR anisotropy induced by the MFR must be a global event, the response of NMs with cutoff rigidities similar to that of HAWC (6–9 GV), during the passage of the MFR was somewhat poor due to the fact that the sensitivity of NMs is lower than that of HAWC in this energy range. These responses are shown in the inset of Figure 10, where the rates of the selected NMs during a three-day period starting on 2016 October 13 are shown. For the sake of clarity, we have added/subtracted an offset to each time profile, and the M<sub>3</sub> rate of HAWC (red line) is divided by 30 to fit the scale.

Even though the behavior of the time profile is different for each monitor, all of them show an increasing trend after day 13 and a more evident decrease after day 14.5. It is interesting to note that the Mexico City NM (magenta line) has a time profile similar to HAWC during and after the second peak, which was caused by low-energy particles (see Section 4.2). The first peak, as mentioned before, was caused by high-rigidity (>15 GV) protons, for which the NM response functions are not well determined (Lockwood 1971).

Due to the fact that neither the initial nor the peak times can be precisely determined, we use the well observed decrease after the second peak to determine the final time of the perturbation on each NM, computed as the mid-time between the maximum and the first change in curvature of the decreasing trend. These times are marked with circles in Figure 10 on the time profiles (inset). The main plot shows the time delay (the fraction of a day after 2016 October 14) of the decrease observed by each NM as a function of its Geolongitude, and shows a clear relationship between the position

of the NM and the final time of the observed interplanetary disturbance. This nonlinear relation is caused by multiple factors such as Earth's rotation, the solar wind velocity at which the MFR is sweeping, the energy of observation, and the detector response function. More detailed study of this effect is required but is out of scope of this paper.

### 4. Flux-rope Model and the GCR Anisotropy

#### 4.1. Fitted MFR Model

Based on visual inspection, the magnetic configuration of the MFR displays a symmetric magnetic field profile. The structure can be described with a very well-organized single MFR with a south-north (SN)  $B_Z$  polarity and positive  $B_Y$ . Thereby, the configuration is defined to be a south-east-north configuration and left-handed (SEN-LH) (see Nieves-Chinchilla et al. 2019, and references therein for details). The MFR reconstruction is based on the circular-cylindrical model described by Nieves-Chinchilla et al. (2016). The model assumes an axially symmetric magnetic field cylinder with twisted magnetic field lines of circular cross section. The magnetic field components in the circular-cylindrical coordinate system are described by

$$B_r = 0, (1)$$

$$B_{y} = B_{y}^{0} \left[ 1 - \left( \frac{r}{R} \right)^{2} \right], \tag{2}$$

$$B_{\phi} = -H \frac{B_{y}^{0}}{|C_{10}|} \frac{r}{R},\tag{3}$$

where the model estimates  $B_y^0$ , the magnetic field at the center of the MFR, and  $C_{10}$ , a measure of the force-freeness along with handedness H (+1 or -1) that indicates whether the MFR is right- or left-handed. The radius of the MFR cross section, R, is a derived parameter (see Equation (5) in Hidalgo et al. 2002) and r is the radial distance from the axis that describes the spacecraft trajectory. The reconstruction technique is based on a multiple regression technique (Levenberg–Marquardt algorithm), which infers the spacecraft trajectory and estimates the orientation of the MFR axis (azimuth and tilt) and the impact parameter  $(y_0)$ .

The reconstruction of the event corroborates the visual inspection, i.e., the structure corresponds to a symmetric MFR with an axis orientation of longitude  $\phi=99^\circ$  and latitude  $\theta=-21^\circ$ . The closest distance of the spacecraft to the axis was  $y_0=-0.0054$  au and the radius R=0.146 au, therefore crossing very close to the center of the MFR ( $y_0/R\approx0.04$ ). H is negative, left-handed. The magnetic field strength at the MFR axis is  $B_y^0=20.7$  nT and the force-freeness parameter  $C_{10}=1.1$  (see Nieves-Chinchilla et al. 2016, for more details).

The twisted reddish curves in Figure 11 represent the fitted MFR at four radial distances from its axis, as quoted in the left side panel. As described in Section 4.2, we used these fitted parameters to model the trajectories (inside the MFR) of the GCRs with different energies and incident angles. The colored curves starting at x = -0.14 au, y = 0 au, and z = 0 au represent these GCR trajectories.

## 4.2. GCR Guiding inside the MFR

As shown in the previous section, the 2016 October ICME had a well-defined magnetic rope topology, ideal for a charged particle to be guided along the MFR axis (governed by the

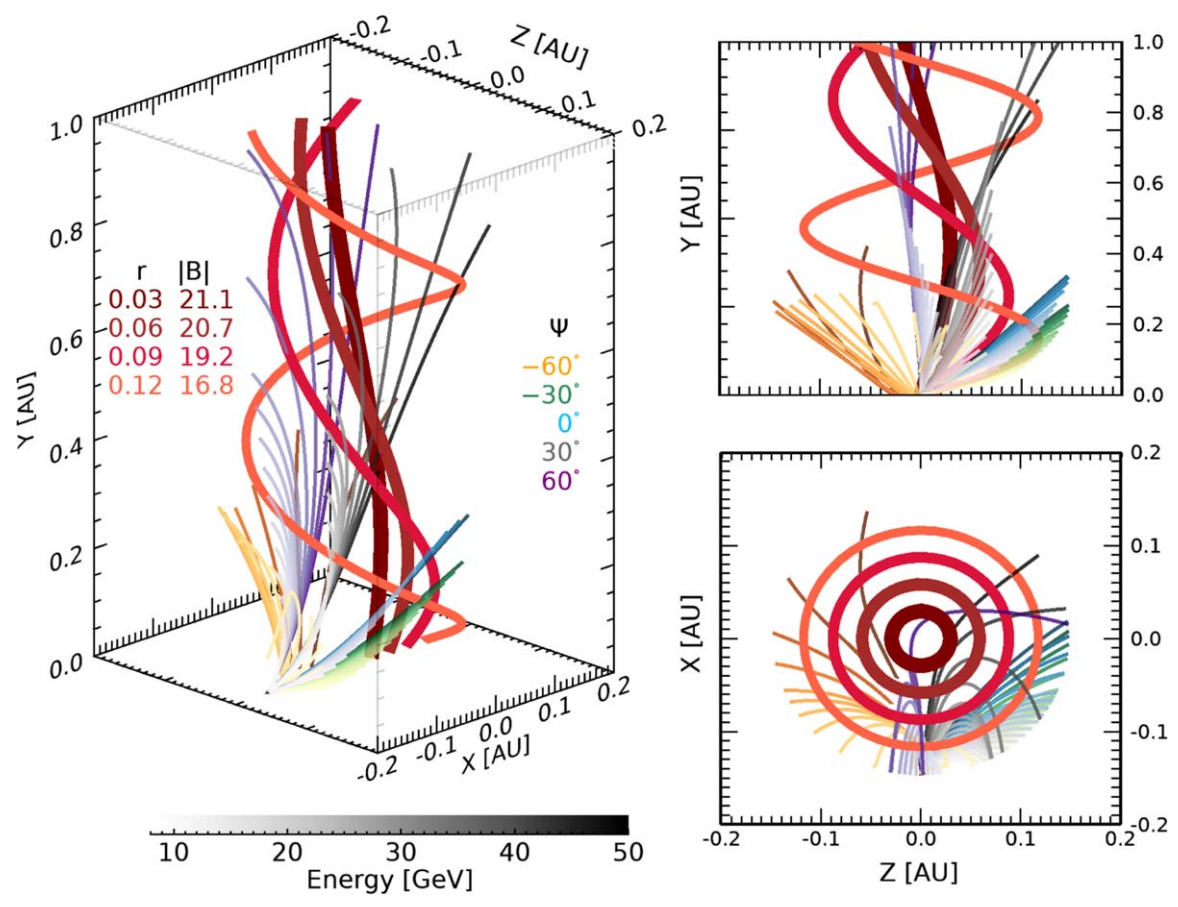


**Figure 11.** Three views of the fitted MFR. In reddish colors we show four magnetic lines of the fitted MFR at the radius (au) and with the magnetic field strengths (nT) annotated on the left side of the left panel. We have simulated the trajectories of GCRs inside this fitted MFR and show some examples at different incident angles ( $\Psi$ , as described in the left panel). The shades of colors represent the GCR energy as shown by the color bar at the bottom left. The right panels show the MFR projections in the ZY (top) and XZ (bottom) planes (see Section 4.2 for details).

Lorentz force). The *B*-field inside the MFR reached a maximum of  $\sim$ 24.64 nT, with a mean value ( $\langle B \rangle$ ) of  $\sim$ 18.56 nT. A GCR entering the MFR experiences a Lorentz force that is maximum while it travels perpendicular to the axis and minimum when its direction is parallel to the axis. The ratio of Larmor radius ( $R_L$ ) to the MFR size ( $S_{\rm MFR}$ ) is shown in Figure 12. The low value of this ratio indicates the capacity of the field to redirect the particles and therefore increase the likelihood of an alignment of the GCRs along the *B*-field (note that this is the field strength along the axis of the MFR).

Furthermore, it should be noted that the *B*-field associated with this MFR had a low turbulence level, which was estimated as  $\sigma_{\rm turb} \leqslant 2\%$ , using a running window method (as explained by Arunbabu et al. 2015). The turbulence level enhances the diffusion of particles, but in this event the turbulence level was low. To quantify this effect, we estimated the ratio of diffusion length ( $L_{\rm diff}$ ) of the particles to  $S_{\rm MFR}$  using the perpendicular diffusion coefficient described in Snodin et al. (2016) with a turbulence level of  $\sigma_{\rm turb} = 2\%$ . The lower value of this ratio of  $L_{\rm diff}/S_{\rm MFR}$  as seen in Figure 12 supports our approximation and illustrates the viability of the model.

To model the trajectory of GCRs inside the MFR we define a coordinate system with the origin at the center of the MFR and the *Y*-axis aligned with the MFR axis. This can be converted from the GSE coordinate system by the rotation operators  $R_Z$  and  $R_Y$  by the angles  $\theta$  and  $\phi$  (see Section 3.3), respectively. We assumed that the MFR has a cylindrical cross section,

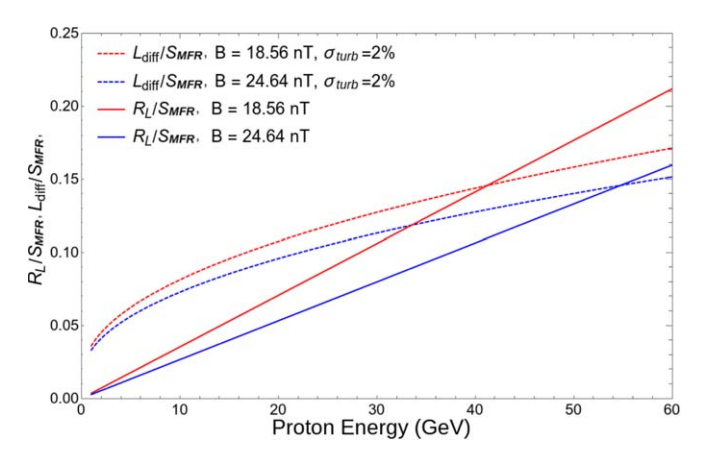


**Figure 12.** The solid lines show the ratio between the Larmor radius  $(R_L)$  and the MFR size, whereas the dashed lines show the ratio between diffusion length and the MFR size for the maximum (blue) and mean (red) magnetic field magnitudes with magnetic turbulence level  $\sigma_{\text{turb}} = 2\%$ .

where the boundary of the MFR lies in the XZ-plane with  $\sqrt{x^2 + z^2} \le 0.5 S_{\rm MFR}$ . The field inside the MFR was modeled using the observations at 1 au and then converted to the coordinate system based on the MFR geometry.

The GCRs entering the MFR are redirected by the Lorentz force  $(\frac{q}{m_p}V \times B)$ . The net deflection is then transformed (relativistically) into the particle frame. When the particle is

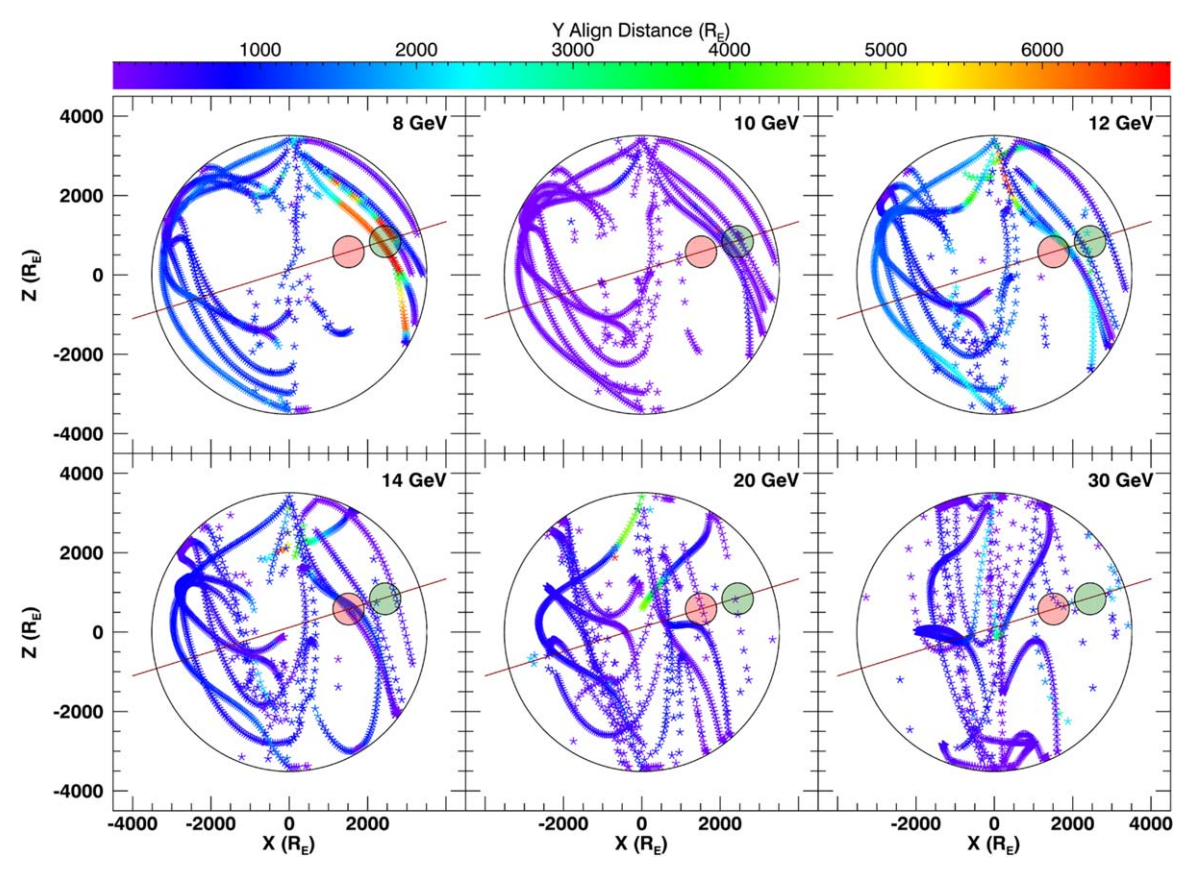


**Figure 13.** Projections on the XZ-plane of the simulated GCR trajectories inside the MFR. Each panel corresponds to particles of different energy (as marked in the top right corner of the panel). Here each point shows the position in XY cross section where it started getting aligned in the axial direction. The color code shows the distance traveled by the particles parallel to the MFR axis. The brown lines show the path of the Earth through the MFR transiting from left to right, and the red and green circles correspond to the approximate duration of the first and second peaks of the HAWC rate excess, respectively.

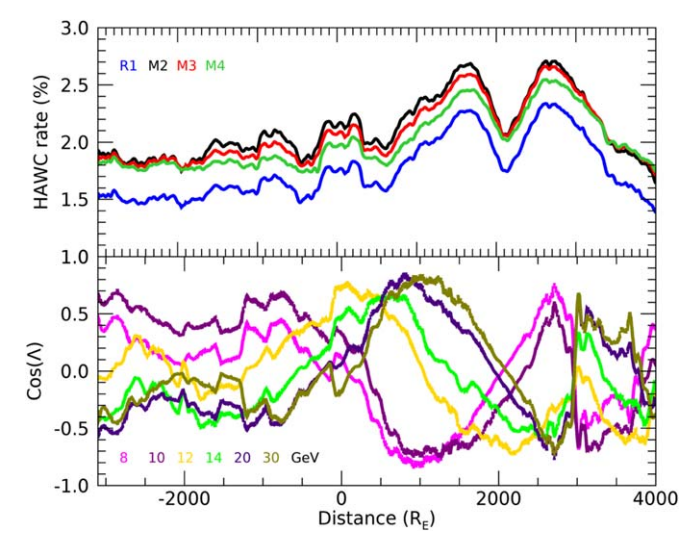


**Figure 14.** The top panel shows the percentage deviation of the HAWC TDC–scaler rates:  $R_1$  (blue), multiplicities  $M_2$ ,  $M_3$ , and  $M_4$  (black, red, and green, respectively) during the passage of the MFR in the Earth's vicinity. The bottom panel shows the cosine of the alignment angle ( $\Lambda$ ) between the HAWC asymptotic direction and the interplanetary B-field during this Earth–MFR encounter; the particle energies are marked with different colors. The distance was computed taking into account the velocity of the MFR.

inside the MFR, its changes in position and velocity are estimated every 100 m of travel. Figure 11 shows a few examples of the simulated particle trajectories inside the fitted MFR.

To estimate the relevant energies of particles that can be guided along the axis of the MFR we performed a simulation, for which we injected protons with energies ranging from 8 to  $100\,\mathrm{GeV}$  entering the MFR at an initial position  $x=-0.5S_\mathrm{MFR},\ y=0,\ \mathrm{and}\ z=0.$  These particles enter the MFR with an incident angle in the XY-plane  $\Psi$ , ranging from  $-70^\circ$  to  $70^\circ$  with an increment of  $1^\circ$ . We tracked the position and direction of each particle inside the MFR by computing the point where it becomes aligned with the axial direction of the MFR (inside the cone with  $85^\circ < \Psi < 95^\circ$ ) and the distance it travels parallel to the axis. We found that that a rather narrow range of rigidity behaves in this manner; specifically, particles of energies higher than  $\sim\!60\,\mathrm{GeV}$  are less likely to be aligned along the axis (see Appendix B for details). Therefore, the enhancement observed by HAWC is due to particles of energies  $\lesssim\!60\,\mathrm{GeV}$  in this model.

As an example, in Figure 11 we show the trajectories inside the MFR of protons with energies between 8 and 50 GeV (marked with color shades) entering the MFR with five different incident angles within the range  $-60^{\circ} < \Psi < 60^{\circ}$  and an increment of  $30^{\circ}$  (marked by the different colors). The entrance position of this example was  $x=-0.5S_{\rm MFR}$ , y=0, and z=0. The incident angle  $\Psi=0$  means that the particle is entering the MFR perpendicular to the Y-axis and the initial velocity of the particle was resolved into perpendicular and parallel components with respect to the MFR axis, using this incident angle as  $V_{\perp}=V\cos\Psi$  and  $V_{\parallel}=V\sin\Psi$ . As expected, the low-energy particles are more affected by the magnetic

topology of the MFR. Particles with median energy and larger  $\Psi$  are more likely to get aligned parallel to the MFR axis.

For completeness and to cover the maximum possible entries of particles into the MFR, we introduced another angle of incidence  $\Xi$  surrounding the MFR in the XZ-plane, varying from 1° to 360° in increments of 1°, and the initial position of entry chosen as  $x = -(0.5S_{MFR})\cos \Xi$ , y = 0, and z = $-(0.5S_{MFR})\sin\Xi$ . If the particles get aligned and travel in the axial direction for more than 60  $R_{\rm E}$  (with  $R_{\rm E}=6357\,{\rm km}$ , the Earth's radius at the equator), the initial position of alignment and the distance traveled parallel to the MFR axis are estimated. The projections of the trajectory of these particles (in the XZ-plane, i.e., in the MFR cross section), with initial energies of 8, 10, 12, 14, 20, and 30 GeV, are shown in Figure 13. The distance traveled parallel to the MFR axis is indicated by the color scale. In this figure, the trajectory of the Earth through the MFR is marked by the brown lines whereas the red and green circles mark the times when the double peak structure was observed by HAWC. Therefore, the number of points inside these circles shows the trajectory of the particles that are likely to be heading toward the Earth at these times. As seen in this figure, our model suggests that the first enhancement detected by HAWC was mainly caused by protons in the energy range 12-30 GeV, whereas the second enhancement was caused by low-energy protons in the range 8-12 GeV.

To reach the lower atmosphere and be detected by HAWC, the GCR anisotropy caused by the MFR (parallel to its axis) must be matched by the HAWC asymptotic directions. Hence, we have estimated the asymptotic direction of these particles using a back-trace method (Smart & Shea 2005) based on IGRF12. The computed directions are shown with colored triangles in Figure 9, where the color code corresponds to the energy. As expected, the low-energy particles are subjected to large deviations inside the geomagnetic field and therefore their asymptotic directions are almost opposite to that of the particles with median energy.

The alignment angle  $(\Lambda)$  between the normal vector of the asymptotic direction  $(\hat{N})$  and the interplanetary *B*-field can be represented as

$$\cos(\Lambda) = \frac{\hat{N} \cdot \mathbf{B}}{|B|}.$$
 (4)

The cosine of  $\Lambda$  reaches the value 1 when **B** is parallel to the HAWC asymptotic direction, allowing the detection of particles of the specific energy (marked with colors in Figure 14). On the other hand, when  $\Lambda < 1$  the particles are not able to reach the detector. It is important to note that during the local minimum at the middle of the double peak structure,  $\cos(\Lambda) \leq 0$  and the parallel distance traveled was  $\leq 2000R_{\rm E}$ (Figure 14) for all particle energies. At this point, the MFR axis was perpendicular to the observing directions of HAWC. Considering this alignment, the first peak of the double peak structure was dominated by particles with energy in the range  $\sim$ 14–30 GeV, whereas the second peak was dominated by lower-energy particles. From this analysis (and as seen in Figure 14) we conclude that the double peak structure observed by HAWC is a geometric effect due to the alignment between the MFR axis and the HAWC asymptotic direction.

#### 5. Discussion

Assuming the intrinsic GCR population is stationary, the local interstellar spectrum of low-rigidity (tens of GV) GCRs is isotropic and constant. Therefore, any change in the intensity at the top of Earth's atmosphere is due to solar modulation. At ground level, the measurements of the GCR spectrum are made using secondary particles, therefore the atmospheric conditions must be taken into account. In this way, once the signal is corrected for atmospheric effects, only one source of GCR fluctuations remains: the Sun.

It is well known that the presence of the largest transients in the SW can cause decreases in the GCR intensity. Although there has been controversy about how the ICME components (shock, sheath, and MFR/CME) are related to this flux modulation (Cane 2000), nowadays it is clear that the decreases in GCRs observed at high energy ( $\gtrsim$ 10 GeV) are mainly attributed to MFRs/ejections and the cumulative diffusion mechanism (Arunbabu et al. 2013), and at lower energies the decreases are caused by the shielding mechanism of the shock–sheath system (Wibberenz et al. 1998).

However, we have described here an interesting phenomenon that has received little attention. This is a local enhancement of the GCR intensity (as opposed to an FD) associated with the passage of an ICME over the Earth.

Such GCR enhancements associated with both FDs and geomagnetic storms were observed and systematically studied (e.g., Kondo et al. 1960), and at that time the thought was that they were a result of changes in cutoff rigidity due to variations in the Earth's magnetic field during geomagnetic storms. This view was eventually discarded because polar stations observed similar enhancements (Dorman et al. 1963).

During the 2016 October event, as shown by the satellite data (Section 3.5) and  $D_{\rm ST}$  index (bottom panel of Figure 3) the major geomagnetic disturbances occurred the day before the HAWC observation, confirming that the GCR enhancement was not caused by the geomagnetic storm or changes in the cutoff rigidity, although we note that the geomagnetic field was still disturbed during the event but by a much smaller amount.

We propose that the GCR enhancement observed by HAWC was due to the anisotropic distribution of GCR particles in the MFR. We believe that the GCRs entered the MFR isotropically (taking into account that the shielding of the shock/sheath region is negligible) and were then guided along the helical geometry of the force-free field for a considerable distance before they escaped (see Figure 1). An anisotropic GCR flux was found during the FD observed in 2013 April. This increase in GCRs detected by the neutron monitor network was analyzed by Tortermpun et al. (2018); these authors attributed the observed anisotropy to guiding center drifts of energetic particles inside an MFR, as predicted by Krittinatham & Ruffolo (2009).

Belov et al. (2015) studied the effects of 99 MCs on the density and anisotropy of 10 GV CRs observed during solar cycles 22 and 23. They found a general increase in the mean anisotropy (2.03% versus 1.38% for MC and non-MC ICMEs, respectively), and more important they found that 20% of the events showed an increase in the CR density. Even though they did not find an explicit relationship between the maximum magnetic field and the CR density extrema, they established that the events with a clear increase in the CR density have a maximum magnetic field <18 nT. We note that the mean value of the magnetic field during the 2016 October event was

~18 nT, and it reached a maximum value of ~24 nT. The difference may be due to the fact that this event took place during the declining phase of solar cycle 24, which was weaker than the previous cycles, and therefore the heliospheric conditions were different. From a theoretical point of view Petukhova et al. (2019, and references therein) developed a model to reproduce the decrease in the local GCR population inside an MFR and found large anisotropies that depend on the MFR geometry and magnetic field strength. Then, to determine the GCR anisotropies during the passage of the MFR observed in 2016 October (see Lockwood 1971, for a discussion of the anisotropies during FDs), we constructed a model to track the trajectories of GCRs inside this specific MFR.

To support the idea of the anisotropic distribution of GCR particles in the MFR, we first recall the special circumstances that gave rise to the HAWC detection.

As discussed in Section 3.1, a quiet filament eruption was the solar origin of the observed MFR. The MFR structure of the associated CME is evident in the SECCHI image in panel (f) of Figure 5. Then, as shown in Section 3.4, the transport of this MFR in the interplanetary medium was surrounded, without interaction, by two high-speed streamers, helping in this way to maintain a helical and strong magnetic field, low density, low turbulence, and a large magnetic/flow pressure ratio. Next, in Section 3.5 we have characterized the response of the B-field in the Earth's magnetosphere due to its interaction with the MFR, and shown that even though the magnetosphere was disturbed during the GCR enhancement, the major disturbances and the geomagnetic storm were observed the previous day, confirming in this way that the observed GCR enhancements are not related to changes in the cutoff rigidity due to the geomagnetic storms.

These facts, and most importantly the alignment between the MFR axis and the asymptotic direction of the HAWC site, allowed the charged particles that were redirected and guided by the MFR (Section 4.2) to reach deep into the low Earth atmosphere to be detected by sensitive ground-level detectors such as HAWC.

### 6. Conclusions

On 2016 October 14 the TDC-scaler system of HAWC registered an unusual increase in the GCR flux. In this work, we have presented evidence that the observed enhancement was caused by an anisotropy generated inside an interplanetary MFR, by the guiding of the GCRs along the axis of the large-scale magnetic structure.

This detection was made possible by a set of unusual circumstances:

- 1. The quiet filament eruption gave rise to the slow CME that reached the Earth with a weak discontinuity (shock) and a relatively quiet sheath region.
- 2. The interaction-free transport of the MFR between two high-speed streamers prevented its deformation because the streamer in front swept the structures of the ambient SW while the one behind did not allow any other faster structure to reach this slow ICME.
- 3. The magnetic field configuration and the low turbulence level allowed the long-distance guiding of the GCR inside the MFR.

- The alignment between anisotropic GCR flux, parallel to the MFR axis, and the asymptotic direction of the HAWC detector
- 5. The high sensitivity achieved by the HAWC TDC–scaler system, which allows the detection of GCR variations with a statistical error <0.01%.

These conditions allowed HAWC to detect the anisotropic flux of GCRs created by the toroidal magnetic field of the MFR.

We acknowledge use of NASA/GSFC's Space Physics Data Facility's OMNIWeb (or CDAWeb or ftp) service, and OMNI data. We are grateful to SOHO, a project of international cooperation between ESA and NASA.

The  $D_{ST}$  (disturbance storm-time) index used in this paper was provided by the WDC for Geomagnetism, Kyoto (http://wdc.kugi.kyoto-u.ac.jp/wdc/Sec3.html).

We acknowledge the support from: the US National Science Foundation (NSF); the US Department of Energy Office of High-Energy Physics; the Laboratory Directed Research and Development (LDRD) program of Los Alamos National Laboratory; L.P. thanks CONACyT grants: 271051, 232656, 260378, 179588, 254964, 258865, 243290, 132197, A1-S-46288, A1-S-22784, cátedras 873, 1563, 341, 323, Red HAWC, México; DGAPA-UNAM grants AG100317, IN111315, IN111716-3, IN111419, IA102019, IN112218; VIEP-BUAP; PIFI 2012, 2013, PROFOCIE 2014, 2015; the University of Wisconsin Alumni Research Foundation; the Institute of Geophysics, Planetary Physics, and Signatures at Los Alamos National Laboratory; Polish Science Centre grant DEC-2018/31/B/ST9/01069, DEC-2017/27/B/ST9/02272; Coordinación de la Investigación Científica de la Universidad Michoacana; Royal Society-Newton Advanced Fellowship 180385. Thanks to Scott Delay, Luciano Díaz, Eduardo Murrieta, and Elsa Noemi Sánchez for technical support.

### Appendix A Magnetospheric Signatures of the Flux Rope

Although the 2016 October event was a slow ICME, it caused a large and unusual disturbance in Earth's magnetospheric as seen by five spacecraft located inside and outside the magnetosphere (see Figures 15–19). Here we present a detailed analysis of these observations.

The arrival of the shock produces a step-like increment in the Earth's magnetic field due to the increment in  $P_{\rm FLOW}$  of the former between the CME-driven shock and the sheath region of the CME (red curve in the fourth panel of Figure 3), which compresses the Earth's magnetic field. This signature can be observed in the first panel of Figures 16–18 (marked as a gray vertical line) corresponding to GOES-15, THEMIS-E, and MMS-1, which were located inside the day-side magnetosphere. THEMIS-C, located in the night-side region of the magnetosheath, also observed the arrival of the shock and the whole structure of the CME (see Figure 19) since the Earth's magnetic field did not permeate that region, as can be corroborated by the upstream/downstream values for different spacecraft (locations) in Table 3.

The detection times of this discontinuity as reported also in Table 3 are in agreement with the relative locations of all the spacecraft as well as with the  $9^{\circ}$  angle of the major axis of the MFR with respect to the *Y*-axis (see Section 3.3), as can be

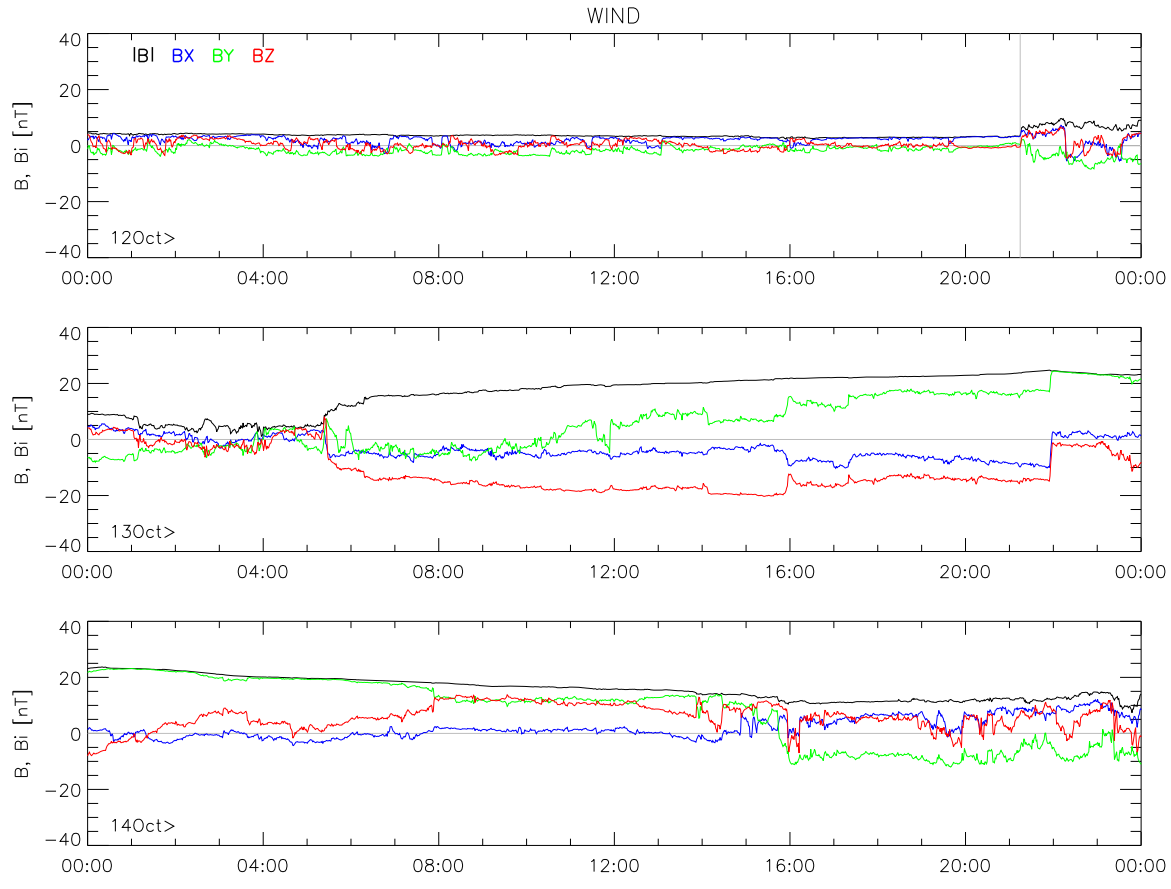


Figure 15. Magnetic field magnitude (black) and its components (colors) in GSE coordinates observed by the Wind spacecraft on October 12 (top), 13 (middle), and 14 (bottom). The vertical gray line indicates the forward shock at 21:15:37 UT on 2016 October 12.

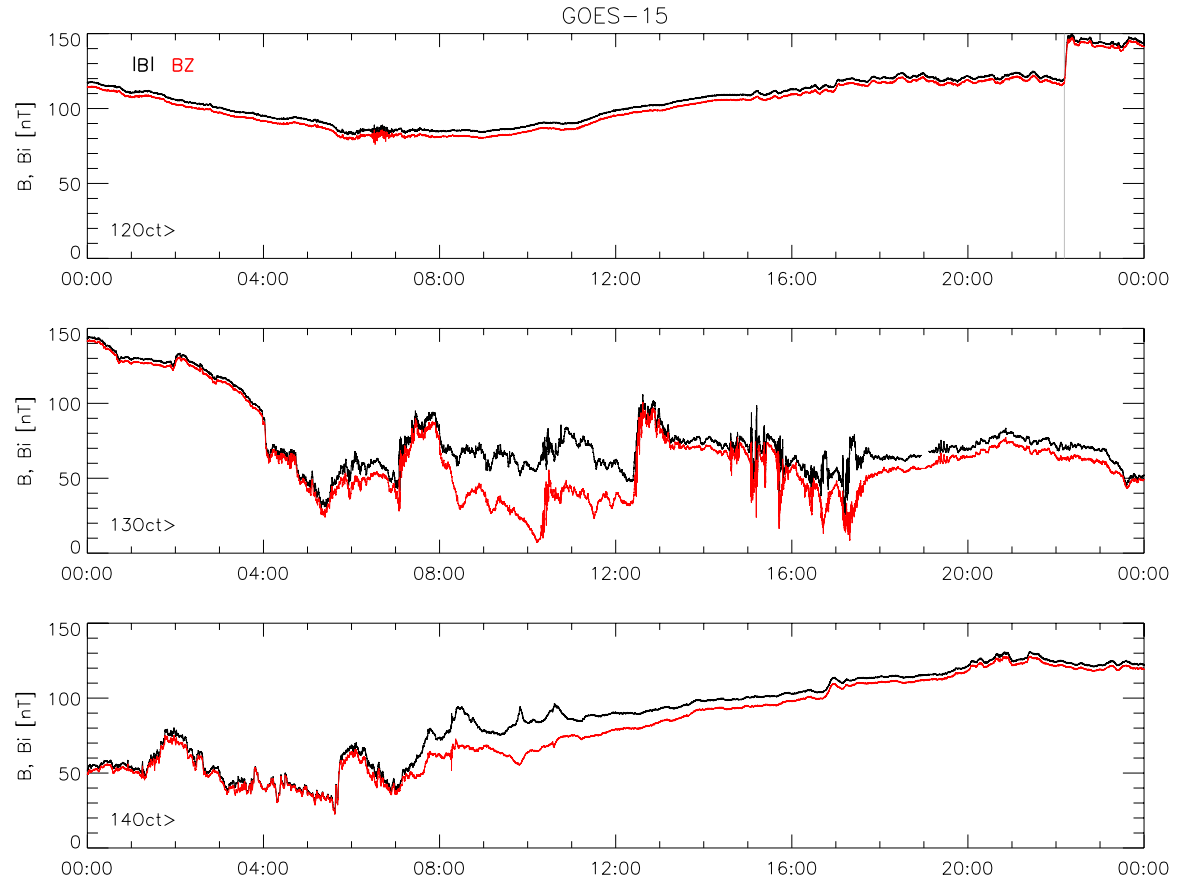
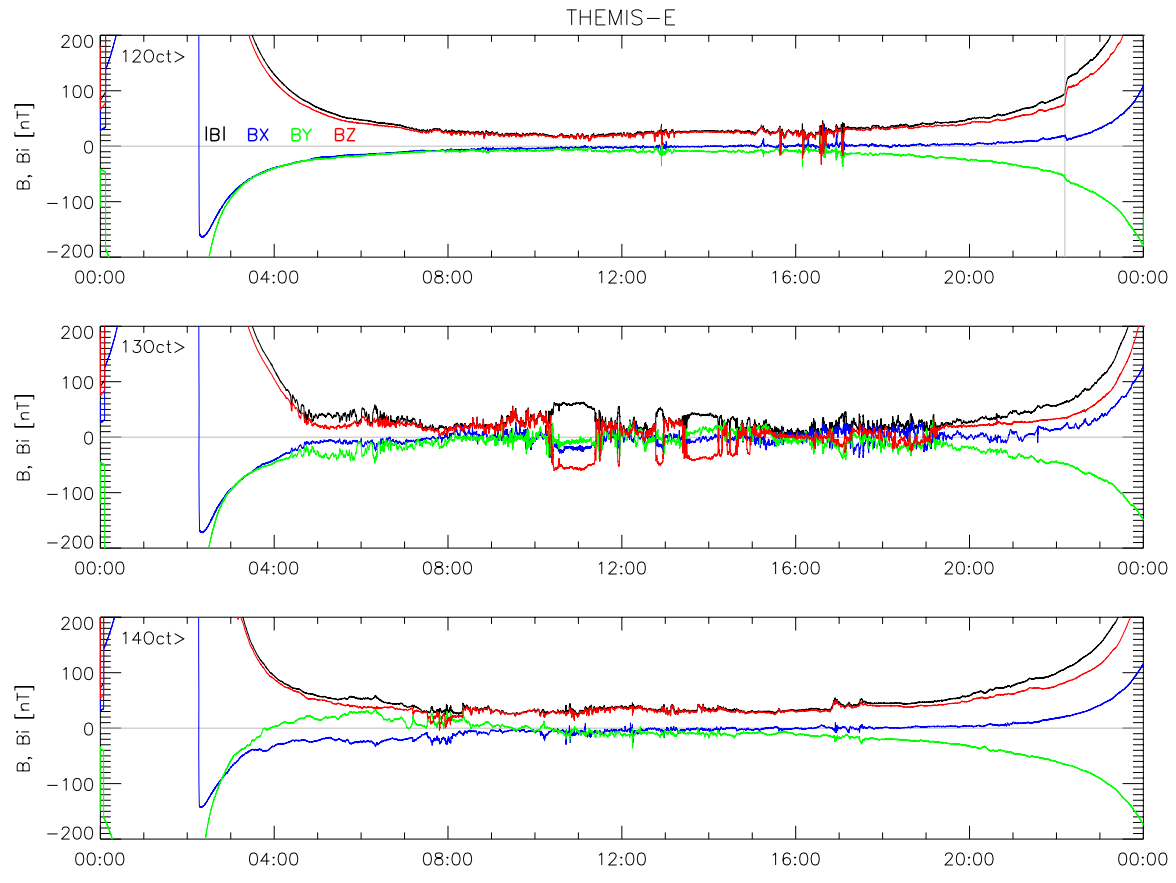


Figure 16. Magnetic field magnitude (black) and  $B_Z$  component (red) in EPN coordinates observed by magnetometer-1 on the GOES-15 spacecraft on October 12 (top), 13 (middle), and 14 (bottom). The vertical gray line indicates the CME shock-related discontinuity at 22:11:51 UT on 2016 October 12.



**Figure 17.** Magnetic field magnitude (black) and its components (colors) in GSE coordinates observed by the THEMIS-E spacecraft on October 12 (top), 13 (middle), and 14 (bottom). The vertical gray line indicates the CME shock-related discontinuity at 22:13:33 UT on 2016 October 12.

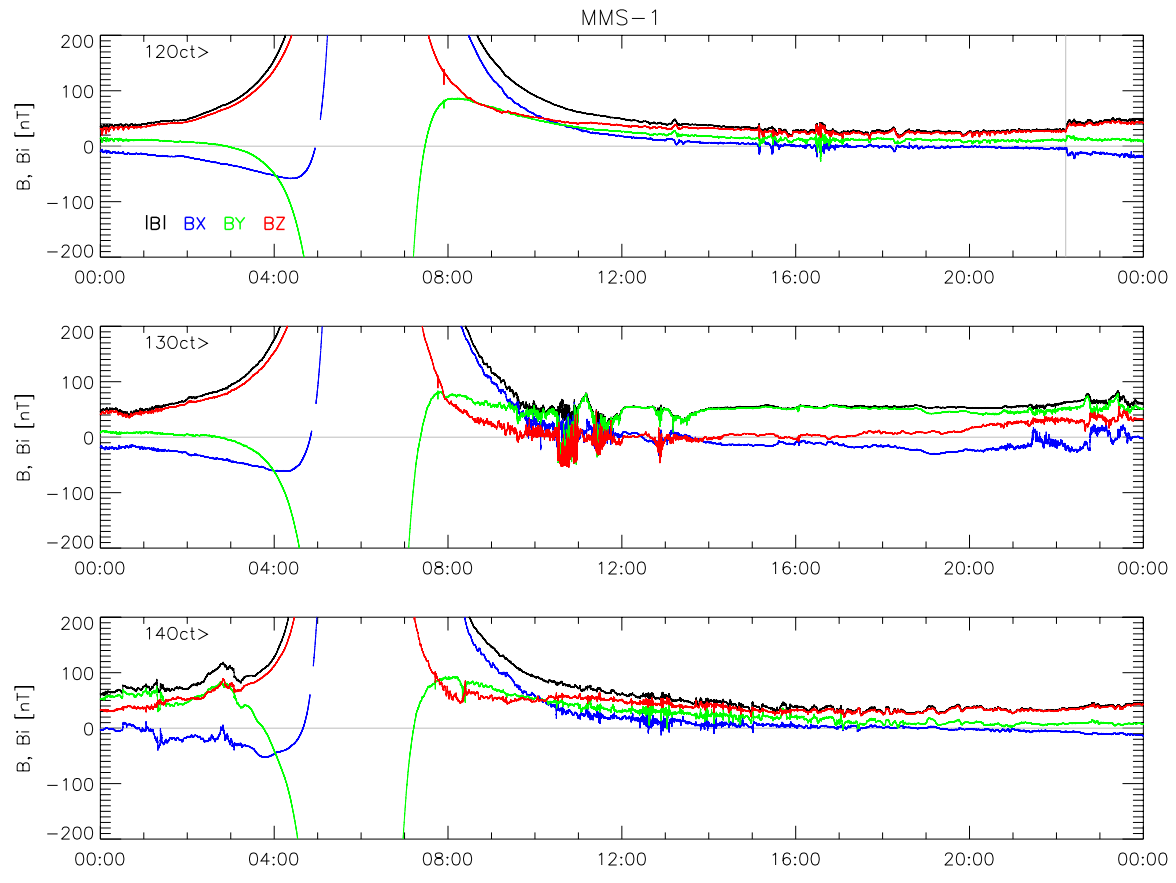


Figure 18. Magnetic field magnitude (black) and its components (colors) in GSE coordinates observed by the MMS-1 spacecraft on October 12 (top), 13 (middle), and 14 (bottom). The vertical gray line indicates the CME shock-related discontinuity at 22:13:52 UT on 2016 October 12.

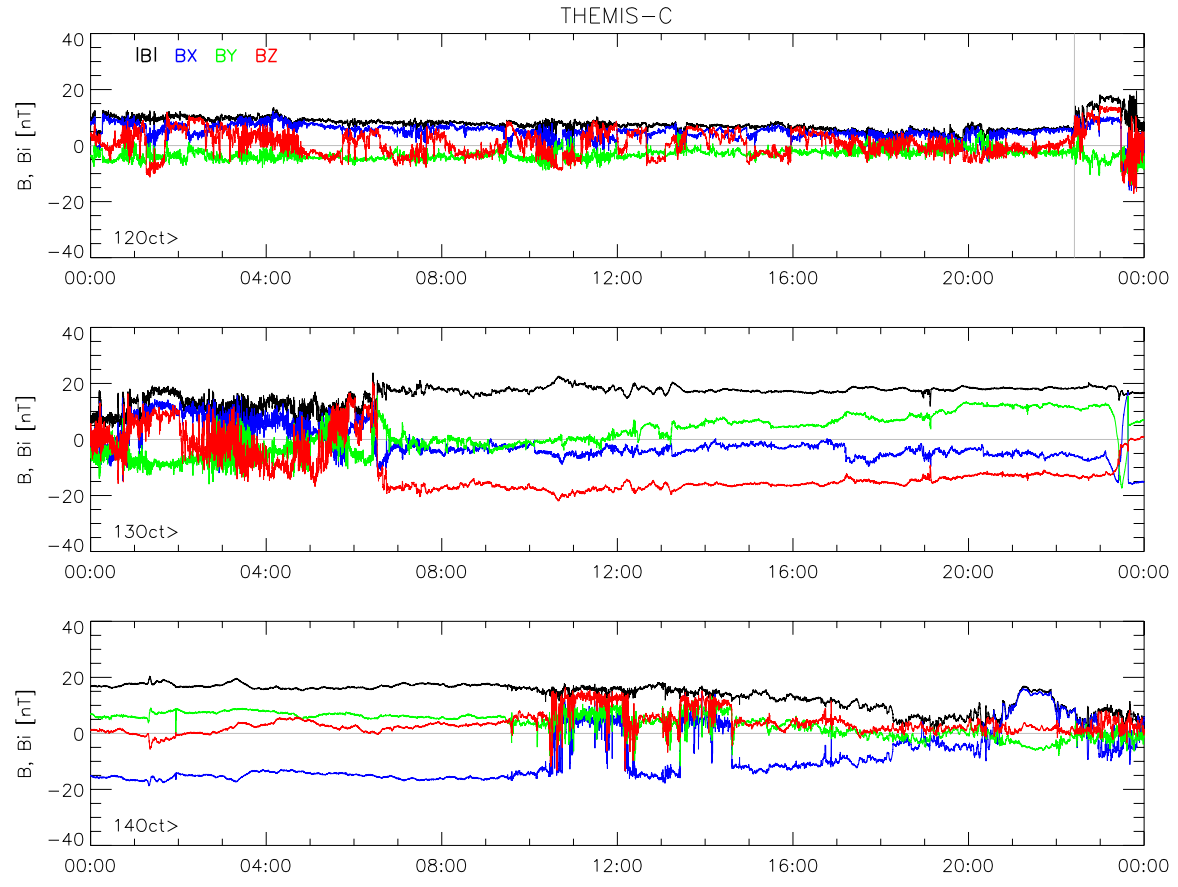


Figure 19. Magnetic field magnitude (black) and its components (colors) in GSE coordinates observed by the THEMIS-C spacecraft on October 12 (top), 13 (middle), and 14 (bottom). The vertical gray line indicates the CME shock-related discontinuity at 22:24:49 UT on 2016 October 12.

observed in the panel corresponding to the *XY*-plane in Figure 7.

The data are in GSE coordinates except for GOES-15, which is presented in EPN coordinates: E (earthward), P (parallel), and N (normal), where N (like our  $B_Z$  component) points northward, perpendicular to the orbital plane of the spacecraft.

# Appendix B Estimating Axial Distance

The simulations of the GCR trajectories were performed for protons of energy ranging from 8 to 100 GeV. Protons were

injected into the MFR at an initial position  $x = -0.5S_{\rm MFR}$ , y = 0, and z = 0. A wide range of incident angles ( $\Psi$ ) in the XY-plane are considered from  $-70^{\circ}$  to  $70^{\circ}$  with an increment of 1°. We checked the alignment (inside the  $85^{\circ} < \Psi < 95^{\circ}$  cone) of particle trajectory along the axis of the MFR, and estimated the distance each particle traveled in the axial direction. The distance traveled in the axial direction for particles of different energy is shown in Figure 20. From this we can conclude that particle of energies >60 GeV are less likely to get aligned with the magnetic topology of the MFR we are considering. The increments in the TDC–scaler rates observed are mainly contributed by lower-energy particles ( $\leq 60$  GeV).

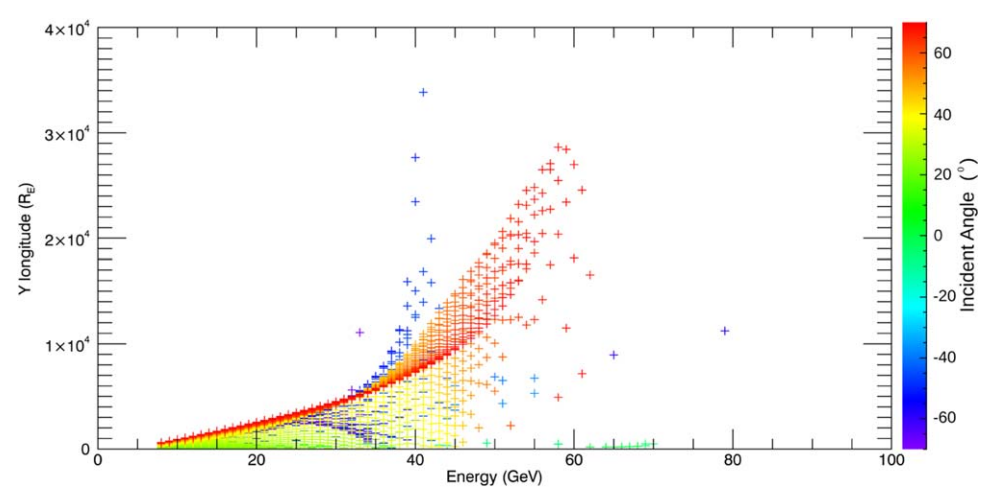


Figure 20. The axial distance traveled by a particle as it enters the MFR at the point  $x = -0.5S_{MFR}$ , y = 0, and z = 0. The color code corresponds to the incident angle in degrees between X and Y at which the particles entered the MFR.

#### **ORCID iDs**

```
S. Akiyama https://orcid.org/0000-0002-7281-1166
K. P. Arunbabu https://orcid.org/0000-0002-3032-663X
H. A. Ayala Solares https://orcid.org/0000-0002-2084-5049
A. Carramiñana https://orcid.org/0000-0002-8553-3302
P. Colin-Farias https://orcid.org/0000-0002-4107-6023
N. Fraija https://orcid.org/0000-0002-0173-6453
M. M. González https://orcid.org/0000-0002-5209-5641
D. Kieda https://orcid.org/0000-0003-4785-0101
A. Lara https://orcid.org/0000-0001-6336-5291
K. Malone https://orcid.org/0000-0001-8088-400X
T. Niembro https://orcid.org/0000-0001-6692-9187
T. Nieves-Chinchilla https://orcid.org/0000-0003-0565-4890
L. Preisser https://orcid.org/0000-0002-5636-2014
J. Ryan https://orcid.org/0000-0003-3534-5968
```

## References

```
Abeysekara, A. U. & HAWC Collaboration 2012, APh, 35, 641
Altukhov, A. M., Kuzmin, A. I., Krimsky, G. F., Skripin, G. V., &
   Chirkov, N. P. 1963, in Proc. ICRC 3, 421 International Cosmic Ray
   Conference (Jaipur, India), 421
Angelopoulos, V. 2008, SSRv, 141, 5
Arunbabu, K. P., Antia, H. M., Dugad, S. R., et al. 2013, A&A, 555, A139
Arunbabu, K. P., Antia, H. M., Dugad, S. R., et al. 2015, A&A, 580, A41
Arunbabu, K. P., Lara, A., Ryan, J. & HAWC Collaboration 2019, in Proc.
   ICRC 36, 36th International Cosmic Ray Conference (ICRC2019)
   (Madison, WI, USA), 1095
Belov, A., Eroshenko, E., Papaioannou, A., et al. 2015, Journal of Physics:
   Conference Series, 632, 012051
Burch, J. L., Moore, T. E., Torbert, R. B., & Giles, B. L. 2016, SSRv, 199, 5
Burlaga, L., Sittler, E., Mariani, F., & Schwenn, R. 1981, JGR, 86, 6673
Cane, H. V. 2000, SSRv, 93, 55
Cantó, J., González, R. F., Raga, A. C., et al. 2005, MNRAS, 357, 572
Cargill, P. J., & Schmidt, J. M. 2002, AnGeo, 20, 879
Chen, C., Liu, Y. D., Wang, R., et al. 2019, ApJ, 884, 90
Colaninno, R. C., & Vourlidas, A. 2009, ApJ, 698, 852
Dere, K. P., Brueckner, G. E., Howard, R. A., Michels, D. J., &
   Delaboudiniere, J. P. 1999, ApJ, 516, 465
Dorman, L. I., Kolomeyets, Y. V., Kozak, L. V., Pivneva, V. T., &
   Sergeyeva, G. A. 1963, Ge&Ae, 3, 293
Duggal, S. P., & Pomerantz, M. A. 1962, PhRvL, 8, 215
Duggal, S. P., Pomerantz, M. A., Schaefer, R. K., & Tsao, C. H. 1983, JGR,
```

```
Fairfield, D. H. 1971, JGR, 76, 6700
Ferreira, S. E. S., & Potgieter, M. S. 2004, ApJ, 603, 744
Filippov, B., Martsenyuk, O., Srivastava, A. K., & Uddin, W. 2015, JApA,
   36, 157
Forbush, S. E. 1937, PhRv, 51, 1108
He, W., Liu, Y. D., Hu, H., Wang, R., & Zhao, X. 2018, ApJ, 860, 78
Hidalgo, M. A., Cid, C., Vinas, A. F., & Sequeiros, J. 2002, JGRA, 107, 1002
Jara Jimenez, A. R., Lara, A., Arunbabu, K. P., Ryan, J. & HAWC
  Collaboration 2019, in Proc. ICRC 36, 36th International Cosmic Ray
  Conference (Madison, WI, USA), 1087
Kaiser, M. L., Kucera, T. A., Davila, J. M., et al. 2008, SSRv, 136, 5
Kay, C., & Opher, M. 2015, ApJL, 811, L36
Kilpua, E., Koskinen, H. E. J., & Pulkkinen, T. I. 2017, LRSP, 14, 5
King, J. H., & Papitashvili, N. E. 2005, JGRA, 110, A02104
Kippenhahn, R., Weigert, A., & Weiss, A. 2012, Stellar Structure and
   Evolution (Berlin: Springer)
Kondo, I., Nagashima, K., Yoshida, S., & Wada, M. 1960, in Proc. ICRC 4,
  International Cosmic Ray Conference (Moscow, Russia), 6208
Krittinatham, W., & Ruffolo, D. 2009, ApJ, 704, 831
Lara, A., Binimelis de Raga, G., Enriquez-Rivera, O. & HAWC Collaboration
  2017, in Proc. ICRC 301, 5th International Cosmic Ray Conference
  (ICRC2017) (Busan, Korea), 80
Lemen, J. R., Title, A. M., Akin, D. J., et al. 2012, SoPh, 275, 17
Light, C., Bindi, V., Consolandi, C., et al. 2020, ApJ, 896, 133
Lockwood, J. A. 1971, SSRv, 12, 658
Luhmann, J. G., Gopalswamy, N., Jian, L. K., & Lugaz, N. 2020, SoPh,
  295, 61
Manchester, W., Kilpua, E. K. J., Liu, Y. D., et al. 2017, SSRv, 212, 1159
Munakata, K., Bieber, J. W., Yasue, S.-i., et al. 2000, JGR, 105, 27457
Niembro, T., Lara, A., González, R. F., & Cantó, J. 2019, JSWSC, 9, A4
Nieves-Chinchilla, T., Jian, L. K., Balmaceda, L., et al. 2019, SoPh, 294,
Nieves-Chinchilla, T., Linton, M. G., Hidalgo, M. A., et al. 2016, ApJ, 823, 27
Nitta, N. V., & Mulligan, T. 2017, SoPh, 292, 125
Nose, M., Iyemori, T., Sugiura, M., & Kamei, T. 2015, in Dst Index, WDC for
  Geomagnetism (Kyoto)
Odstrcil, D., Riley, P., & Zhao, X. P. 2004, JGRA, 109, A02116
Parker, E. N. 1965, P&SS, 13, 9
Pesnell, W. D., Thompson, B. J., & Chamberlin, P. C. 2012, SoPh, 275, 3
Petukhova, A. S., Petukhov, I. S., & Petukhov, S. I. 2019, JGRA, 124, 19
Raga, A. C., Navarro-González, R., & Villagrán-Muniz, M. 2000, RMxAA,
   36, 67
Richardson, I. G., & Cane, H. V. 2010, SoPh, 264, 189
Richardson, I. G., & Cane, H. V. 2011, SoPh, 270, 609
Rockenbach, M., Dal Lago, A., Gonzalez, W. D., et al. 2011, GeoRL, 38,
  L16108
Roelof, E. C., & Sibeck, D. G. 1993, JGR, 98, 21421
Sarp, V., Kilcik, A., Yurchyshyn, V., Ozguc, A., & Rozelot, J.-P. 2019, SoPh,
Schmieder, B., Aulanier, G., & Vršnak, B. 2015, SoPh, 290, 3457
```

Schwenn, R., dal Lago, A., Huttunen, E., & Gonzalez, W. D. 2005, AnGeo, 23, 1033

Sheeley, N. R. J., Harvey, J. W., & Feldman, W. C. 1976, SoPh, 49, 271
Sinha, S., Srivastava, N., & Nandy, D. 2019, ApJ, 880, 84
Smart, D. F., & Shea, M. A. 2005, AdSpR, 36, 2012

Snodin, A. P., Shukurov, A., Sarson, G. R., Bushby, P. J., & Rodrigues, L. F. S. 2016, MNRAS, 457, 3975

Snyder, C. W., Neugebauer, M., & Rao, U. R. 1963, JGR, 68, 6361

Sugiura, M. 1964, Ann. Int. Geophys. Yr., 35, https://ntrs.nasa.gov/citations/19650020355

Tortermpun, U., Ruffolo, D., & Bieber, J. W. 2018, ApJL, 852, L26 Wibberenz, G., le Roux, J. A., Potgieter, M. S., & Bieber, J. W. 1998, SSRv, 83, 309

Wilson, L. B. I., Stevens, M. L., Kasper, J. C., et al. 2018, ApJS, 236, 41 Yoshida, S. 1959, Natur, 183, 381

Zurbuchen, T. H., & Richardson, I. G. 2006, SSRv, 123, 31